MOX-Report No. 05/2026

A fictitious domain formulation based on hierarchical model reduction applied to drug-eluting stents

Ranno, A.; Ballarin, F.; Lespagnol, F.; Zunino, P.; Perotto, S.

MOX, Dipartimento di Matematica
Politecnico di Milano, Via Bonardi 9 - 20133 Milano (Italy)

mox-dmat@polimi.it https://mox.polimi.it

A fictitious domain formulation based on hierarchical model reduction applied to drug-eluting stents

Anna Ranno[†], Francesco Ballarin[‡], Fabien Lespagnol[§],
P. Zunino[#], S. Perotto[#]

January 12, 2026

[†] Chair for Computational Analysis of Technical Systems
RWTH Aachen University, Aachen, Germany
ranno@cats.rwth-aachen.de

[‡] Department of Mathematics and Physics
Università Cattolica del Sacro Cuore, Brescia, Italy
francesco.ballarin@unicatt.it

§ Institut Montpellierain Alexander Grothendieck
Université de Montpellier, Montpellier, France
fabien.lespagnol@umontpellier.fr

MOX – Modellistica e Calcolo Scientifico, Dipartimento di Matematica
Politecnico di Milano, Milano, Italy
{paolo.zunino,simona.perotto}@polimi.it

Abstract

This paper presents a novel combination of the Fictitious Domain (FD) approach with the Hierarchical Model (HiMod) reduction for the simulation of the hemodynamics in an artery with a drug-eluting stent. Classical finite element methods are computationally expensive due to the geometrical complexity of stented arteries. The FD approach merges stent and lumen domains into a single computational domain, weakly imposing boundary conditions on the stent-lumen interface via Lagrange multipliers. However, the FD technique can lead to inaccurate solutions when dealing with non-conforming grids. In contrast, a HiMod formulation offers flexibility in tuning accuracy and computational cost but struggles with non-smooth domains like stented arteries. To address these limitations, we combine the FD and HiMod approaches, using a reduced stent-lumen interface condition to simplify implementation while maintaining accuracy. This combined approach is tested on an advection-diffusion equation to model drug elution into the bloodstream. For proof-of-concept, we use a simplified axisymmetric geometry comprising an idealized artery segment and a ring-shaped stent. Finally, we extend our analysis to include more realistic blood flow conditions and conduct a sensitivity analysis of drug concentration with respect to ring spacing. The numerical results demonstrate the effectiveness of the proposed approach.

Keywords: hemodynamics, drug-eluting stents, fictitious domain, hierarchical model reduction.

1 Introduction

Vascular stents are biomedical devices designed to keep stenosed blood vessels open, thus playing a critical role in the treatment of cardiovascular diseases. These devices interact with the blood flow

in a complex way. In particular, vascular stents may alter the blood dynamics near the vascular wall, which can affect the shear stress [49] as well as the distribution of blood cells and nutrients [35]. Furthermore, stent implantation can lead to serious side effects, such as in-stent restenosis [15]. Thus, an accurate in-silico prediction of such procedure outcomes, prior to stent implantation, is crucial to help interventional cardiologists make informed decisions. More specifically, an integrated approach, which includes mechanical analysis of stent expansion, interaction with the artery, characterization of blood flow, disturbances in fluid dynamics, and subsequent tissue remodeling [30], is essential to predict the efficacy of endovascular therapies.

In recent decades, numerical models have become invaluable tools for studying stent implantation [40]. The early models, limited by computational resources, dealt with simplified scenarios and idealized arteries [54]. Today, advances in computational capabilities have allowed these models to address complex clinical scenarios, including multiple stents in bifurcated or curved arteries [8]. Recent literature has witnessed the introduction of image-based methods for reconstructing realistic coronary vessel geometries, enhancing the precision of numerical models [52]. Furthermore, significant advancements in the structural and fluid dynamics modeling of arteries have been achieved [41, 53], for instance to better understand how therapeutic chemicals interact with the vascular wall through the bloodstream when dealing with drug-eluting stent (DES) devices [37].

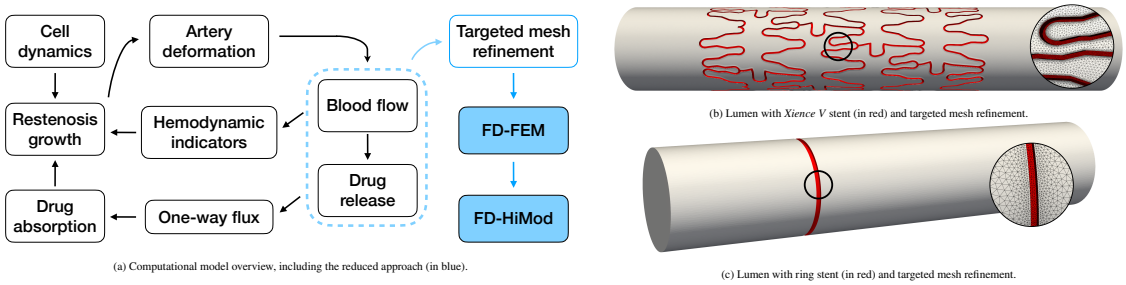

(a) Computational model overview, including the reduced approach (in blue).

(b) Lumen with *Xience V* stent (in red) and targeted mesh refinement.

(c) Lumen with ring stent (in red) and targeted mesh refinement.

Figure 1: Scheme illustrating the main steps involved in modeling arteries with DES and restenosis, including the role of the proposed fictitious domain (FD) and model reduction (HiMod) approach. For the proof-of-concept, we transition from a complex stent, such as the *Xience V*, to a simplified one-ring stent.

However, stented artery modeling still poses significant challenges. First of all, modeling multi-physics processes, such as in-stent restenosis, includes complex interaction among blood flow, stent and artery wall. A sketch of the main phenomena involved in arteries with DES and restenosis [50] is shown in Figure 1a (leftmost 3 columns). It is essential to include various cell types, such as smooth muscle and endothelial cells, and growth factors (e.g., PDGF and TGF) [36] to model neointima growth. DES release drug both by direct contact with the arterial wall and into the bloodstream, where it is subsequently absorbed by the artery. Drug absorption, along with cell dynamics and hemodynamic disturbances, influences predictions of restenosis-related arterial growth. Additionally, restenosis further disrupts hemodynamics, necessitating updates to the stented lumen. From a modeling viewpoint, the Navier-Stokes equations are widely used to manage the hemodynamics. For cell dynamics, two main approaches are recurrent, i.e., agent-based models, which are limited to 2D scenarios [11], and advection-diffusion-reaction equations [24], which are used in a 3D continuum setting and are also suitable for modeling drug release. Advection-diffusion-reaction equations provide an ideal framework for describing the transport and interaction of chemicals, offering a versatile approach applicable to various biomedical contexts.

As a second challenge in modeling arteries with DES, in addition to stent deployment, we highlight the need to preserve a detailed geometric representation while reducing model complexity. Models have been developed to investigate drug release from stents [37], utilizing approaches ranging from

one-dimensional [38, 47] and two-dimensional [28, 2], to complex three-dimensional representations [12, 27]. A possibility is to use a targeted mesh refinement (see Figure 1a, first step in right-most column), as higher accuracy is required near the stent struts (see, e.g., Figure 1b). These regions are identified a priori, particularly when addressing different levels of stent indentation [10]. However, targeted mesh refinement can reduce computational costs only moderately [49].
As an alternative, dimensional model reduction has been used to provide detailed geometrical and physical descriptions of stents, facilitating cost-effective calculations [55]. Recent approaches using mixed-dimensional and fluid-beam interaction models address the detailed geometric issue by preserving the intricate stent design while simplifying the complexity of surrounding flow and drug transport models [55, 23]. These methods build upon fictitious domain (FD) methods, which have been extensively used to address problems involving complex geometries [4, 31, 19]. A comprehensive review of FD approaches in combination with the finite element method (FEM) and its enhancements can be found in a recent work by Regazzoni [51]. In the FD approach, to simplify the geometrical complexity, two intersecting domains are merged into one, while preserving the interface between the parts. Various techniques are adopted to impose boundary conditions on this interface. Among the others, Lagrange multipliers (LM) have been successfully applied to enforce Dirichlet boundary conditions, proving to be effective in multiple applications [6]. In the specific case of modeling stented arteries, the artery domain is much larger than the stent, which acts as an obstacle in the main domain. A previous work shows that the LM approach becomes particularly effective as the obstacle size decreases [5].

In this work we employ a variant of the FD method [20] – specifically derived for addressing fluid-beam interaction problems by means of reduced-order interface coupling conditions [25, 5, 32] – to model the stent presence in the artery, while reducing the computational effort associated with drug elution modeling through the adoption of a model order reduction technique [18, 26, 48]. To this end, we properly combine the FD approach with a Hierarchical Model (HiMod) reduction (see Figure 1a, second and third step in right-most column), which proved to be an ideal tool to surrogate models with an intrinsic (geometrical or physical) directionality, in different application contexts, such as advection-diffusion-reaction phenomena [45, 1, 14, 43, 46, 33, 34, 9], blood flow modeling [21, 7, 44], linear acoustics [17], and electromagnetism [16]. The advantage of HiMod reduction lies in the use of separation of variables, allowing different levels of accuracy between the main and the transverse direction. This separation allows for numerical approximations to be specifically tailored to distinct features of the problem, optimizing computational efficiency while preserving essential dynamics. However, HiMod is inherently characterized by limitations on the geometry of the computational domain. For example, sharp angles or bifurcations are difficult to model with a HiMod reduction. Similarly, stent structures and the resulting stented lumen geometry generally do not meet such geometrical requirements. The combination of HiMod with a FD approach allows us to overcome this limitation. In addition, the reduced LM method helps enforce non-matching constraints across the stent-fluid interface [5, 32].
The objective of this work is to demonstrate the effectiveness of combining FD and HiMod reduction techniques in simplifying drug-eluting stent modeling, ensuring a comprehensive and robust treatment of both the drug release and fluid model. In more detail, HiMod reduction is applied to an advection-diffusion equation that models drug elution, while we adopt a simplified one-ring device geometric configuration, given the proof-of-concept nature of this study (see Figure 1c).

The manuscript is organized as follows. Section 2 introduces the computational model for the drug release from a DES, along with the associated axisymmetric formulation, thus reducing the ring stent benchmark case to a 2D problem. Section 3 constitutes the core of the paper, initially presenting the FD formulation with a reduced interface in a FEM framework, followed by the combination with HiMod reduction. Section 4 presents the results both for a benchmark case with one-ring stent and for a production case with three rings. In particular, in Section 4.1, we analyze both accuracy and convergence, with and without HiMod, for the benchmark case, while in Section 4.2, we perform a sensitivity analysis for scenarios with multiple rings and realistic flow conditions, discussing the key

observations in Section 4.3. Finally, we draw some conclusions in Section 5.

2 Computational model of a drug-eluting stent

In this section, we present the model for drug elution from a stent using an advection-diffusion equation, where the advection field is given by the solution of the Navier-Stokes equations. In particular, in Section 2.1 we move from a 3D setting to an axisymmetric 2D setup for simplicity.

Concerning the computational domain, we consider an idealized coronary artery with a DES. The lumen segment without DES coincides with a 10 mm long cylinder, with a 2 mm diameter. We assume perfect contact between stent and artery wall (i.e., no indentation[10]) and that the stent is completely contained within the artery segment. Furthermore, we consider a simplified stent geometry made of rings with square cross-section and thickness $\epsilon = 0.1$ mm. We denote by $\Omega_{\hat{\mathbf{z}}}$ the domain of the artery lumen and by $\widehat{\omega}_\epsilon$ the volume enclosed by the stent structure. Both the stent and the artery are embedded in a 3D Cartesian system of coordinates, with $\hat{\mathbf{z}} = (x, y, z)$. The perforated domain $\Omega_{\hat{\mathbf{z}},\epsilon} = \Omega_{\hat{\mathbf{z}}} \setminus \widehat{\omega}_\epsilon$ is the spatial domain of a lumen segment with a DES, where the stent acts as obstacle to the blood flow, and $\partial\Omega_{\hat{\mathbf{z}},\epsilon}$ is the boundary of the perforated domain. It is important to highlight that we are only considering the drug released from the stent into the blood stream. Thus, the drug released by direct contact with the artery wall is neglected and the relevant stent surface is $\widehat{\Gamma}_S = \partial\widehat{\omega}_\epsilon \backslash \partial\Omega_{\hat{\mathbf{z}}}$. Furthermore, the interface between lumen and artery wall is $\widehat{\Gamma}_{w,\epsilon}$ in the perforated domain, but, the complete artery wall is given by $\widehat{\Gamma}_w$. A visual sketch is provided in Figure 2.

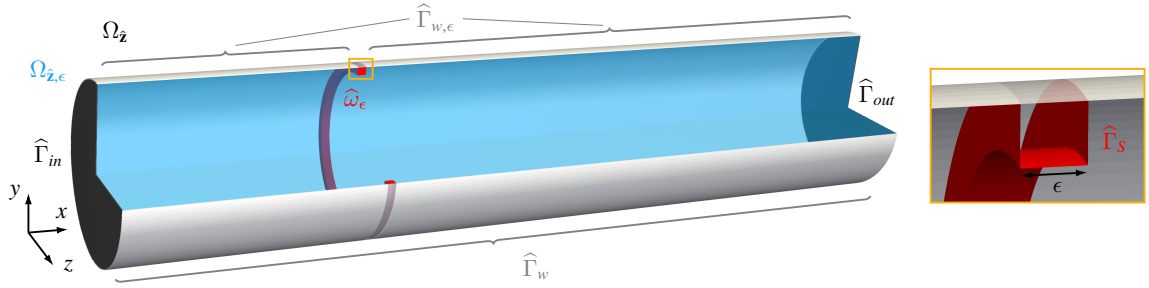

Figure 2: Representation of an idealized 3D artery lumen (in blue) with a ring stent (in red) and corresponding domain and boundary notations.

In general, drug release from the stent into the blood stream is modeled with an advection-diffusion equation for a given diffusion, D, here assumed constant, and an advective field, $\mathbf{u}$. Experimental results of DES show that drug is released over the time span of few months. Hence, we consider the drug concentration to be in a quasi-steady regime within a one day time horizon and drop the time dependence[50]. Thus, the drug release reference model is given by

$$\begin{cases} -D\Delta c + \mathbf{u}\cdot\nabla c = 0 & \text{in } \Omega_{\hat{\mathbf{z}},\epsilon} \\ c = c_0 & \text{on } \widehat{\Gamma}_S \\ c = 0 & \text{on } \widehat{\Gamma}_{in} \\ D\nabla c\cdot\mathbf{n} = 0 & \text{on } \widehat{\Gamma}_{out} \\ c = 0 & \text{on } \widehat{\Gamma}_{w,\epsilon}, \end{cases} \tag{1}$$

with $c = c(\hat{\mathbf{z}})$ the drug concentration in the lumen, c_0 the drug load on the stent surface $\widehat{\Gamma}_S$, $\widehat{\Gamma}_{in}$ and $\widehat{\Gamma}_{out}$ the inflow and outflow boundary, $\mathbf{n}$ the outward unit normal vector to the domain boundary,

where we have assumed that no drug is transported upstream the stent. The artery wall, $\widehat{\Gamma}_{w,\epsilon}$, is here treated as a perfect sink. As an alternative, it may model a membrane in equilibrium with zero flux. This is equivalent to replacing condition $c = 0$ on $\widehat{\Gamma}_{w,\epsilon}$ in (1) with homogeneous Neumann boundary data. The advective field, $\mathbf{u}$, here assumed divergence-free, can be chosen arbitrarily to ensure a global Péclet number, $\mathbb{P}\mathrm{e}$, strictly less than one, or it can coincide with the solution to the incompressible Navier-Stokes equations

$$\begin{cases} \rho\mathbf{u}\cdot\nabla\mathbf{u} - \nabla\cdot(2\mu\ \mathbf{E}(\mathbf{u})) + \nabla p = \mathbf{0} & \text{in } \ \Omega_{\hat{\mathbf{z}},\epsilon} \\ \nabla\cdot\mathbf{u} = 0 & \text{in } \Omega_{\hat{\mathbf{z}},\epsilon} \\ \mathbf{u} = \mathbf{0} & \text{on } \widehat{\Gamma}_S \\ \mathbf{u} = \mathbf{f} & \text{on } \widehat{\Gamma}_{in} \\ (2\mu\ \mathbf{E}(\mathbf{u}) - pI)\mathbf{n} = \mathbf{0} & \text{on } \widehat{\Gamma}_{out} \\ \mathbf{u} = \mathbf{0} & \text{on } \widehat{\Gamma}_{w,\epsilon}, \end{cases} \tag{2}$$

to model the blood flow in the coronary artery, with $\mathbf{u}(\hat{\mathbf{z}}) = [u_x(\hat{\mathbf{z}}), u_y(\hat{\mathbf{z}}), u_z(\hat{\mathbf{z}})]^T$ the velocity vector, $p = p(\hat{\mathbf{z}})$ the pressure, $\mathbf{E}(\mathbf{u}) = \frac{1}{2}\left(\nabla\mathbf{u} + \nabla\mathbf{u}^T\right)$ the strain rate tensor, ρ and μ the blood density and dynamic viscosity, respectively – both considered constant throughout the paper – and I the identity matrix. We have assumed here a Newtonian constitutive law for the blood flow although the model can be easily adapted to a shear-thinning regime. The velocity, $\mathbf{f} = \mathbf{f}(\hat{\mathbf{z}})$, imposed at the inflow has a parabolic profile whose magnitude depends on the characteristic flow rate in a right coronary artery [49]. Given the quasi-steady behaviour of the drug release, the pulsatile blood flow is averaged to 1 ml/s, while any elastic response of the arterial wall to the blood pressure is neglected [39].

2.1 Axisymmetric formulation of the prototype stent problem

Due to the approximately cylindrical shape of arteries, we rewrite problem (1) in a cylindrical coordinate system, using the standard coordinate transformation $\hat{\mathbf{z}} = (x, y, z) \to \mathbf{z} = (x, r, \varphi)$, with r and φ the radial and the azhimutal coordinate, respectively, and where the following relation holds: $(x, y, z) = (x, r\cos(\varphi), r\sin(\varphi))$. Thanks to the artery and stent geometrical assumptions, the computational domain is axisymmetric, i.e., symmetric with respect to rotations around the x-axis. Thus, the axisymmetric concentration $c = c(x, r)$, velocity $\mathbf{u} = \mathbf{u}(x, r) = [u_x(x, r), u_r(x, r)]^T$ and pressure $p = p(x, r)$ are independent of the coordinate φ[3]. This simplification allows us to reduce the computational domain by one dimension and to consider only the half section $\Omega = \Omega_{\mathbf{x},\epsilon} \cup \omega_\epsilon$, with $\mathbf{x} = (x, r, 0) = (x, r)$, after assuming that any section is equivalent in terms of the azhimutal coordinate φ. Thus, we denote by ω_ϵ the 2D axisymmetric stent, and by Γ_{in}, $\Gamma_{w,\epsilon}$, Γ_S, Γ_{out}, and Γ_{axi} the axisymmetric boundaries of the corresponding perforated domain $\Omega_{\mathbf{x},\epsilon}$, where Γ_{axi} is the boundary along the symmetry axis resulting from the choice of the half section (see Figure 3 for a sketch). On Γ_{axi} we impose a zero flux condition ($D\nabla c\cdot\mathbf{n} = 0$) for the concentration in (1), and an impenetrability condition ($\mathbf{u}\cdot\mathbf{n} = 0$) for the velocity $\mathbf{u}$ in (2). Concerning the other boundary portions, we retain the same conditions as in (1) and (2), including the non homogeneous data c_0 on Γ_S and $\mathbf{f}$ on Γ_{in}.

A reformulation of the advection-diffusion and of the Navier-Stokes equations in (1) and (2) within the new geometric framework is obtained by introducing the definition of the gradient, the divergence and the Laplacian axisymmetric operators in cylindrical coordinates [29], being $\nabla = (\partial_x, \partial_r)$, $\nabla\cdot = \left(\partial_x, \frac{1}{r} + \partial_r\right)$, $\Delta = \partial_{xx} + \partial_{rr} + \frac{1}{r}\partial_r$. Moreover, we remark that the volume integral $\int_{\Omega_\mathbf{z}} f(\mathbf{z})\, d\Omega_\mathbf{z} = \int_0^L \int_0^R \int_0^{2\pi} f(x, r, \varphi) r\, dx\, dr\, d\varphi$ over the generic 3D domain $\Omega_\mathbf{z}$ in cylindrical coordinates simplifies to $2\pi \int_0^L \int_0^R f(x, r) r\, dx\, dr$ for an azimuthally-invariant function f such that $f(x, r, \varphi) = f(x, r)$ for any φ. As a consequence, the dimension reduction associated with an axisymmetric formulation results in a simpler expression for the integrals, thus significantly simplifying the numerical implementation.

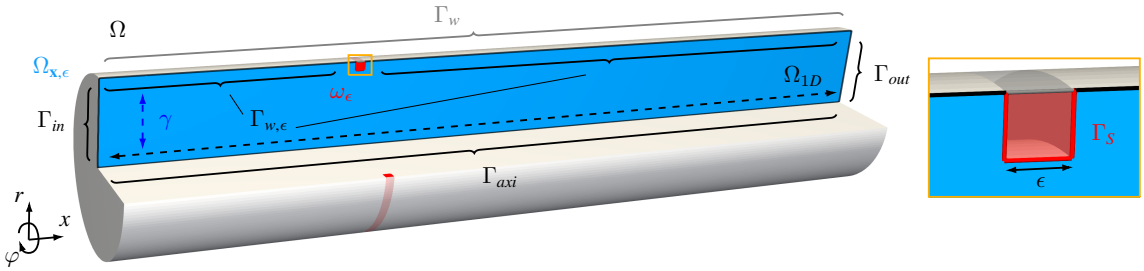

Figure 3: Axisymmetric 2D artery lumen (in blue) with a ring stent (in red) and corresponding domain and boundary notations.

As a starting point in setting up the method proposed in this work, we consider the weak formulation of the axisymmetric counterpart of problems (1) and (2). To this end, we introduce the appropriate function framework, starting from the space

$$L^2_r(\Omega_{\mathbf{x},\epsilon}) = \left\{ v : \Omega_{\mathbf{x},\epsilon} \to \mathbb{R} \ : \ \left(\int_{\Omega_{\mathbf{x},\epsilon}} \left| v(x,r) \right|^2 \, r \, dx \, dr \right)^{1/2} < +\infty \right\} \tag{3}$$

together with the space $H^1_r(\Omega_{\mathbf{x},\epsilon})$ of the functions in $L^2_r(\Omega_{\mathbf{x},\epsilon})$ with gradient belonging to $\left[L^2_r(\Omega_{\mathbf{x},\epsilon})\right]^2$. Thus, we define the spaces[3]

$$\begin{aligned}
W_x(\Omega_{\mathbf{x},\epsilon}) &= \left\{ w_x \in H^1_r(\Omega_{\mathbf{x},\epsilon}) \ : \ w_x = 0 \text{ on } \Gamma_D^{NS} \right\}, \\
W_r(\Omega_{\mathbf{x},\epsilon}) &= \left\{ w_r \in H^1_r(\Omega_{\mathbf{x},\epsilon}) : \left(\int_{\Omega_{\mathbf{x},\epsilon}} |w_r(x,r)|^2 \, \frac{1}{r} \, dx \, dr \right)^{\frac{1}{2}} < +\infty, \ w_r = 0 \text{ on } \Gamma_D^{NS} \right\}, \\
Q(\Omega_{\mathbf{x},\epsilon}) &= \left\{ q \in L^2_r(\Omega_{\mathbf{x},\epsilon}) \ : \ \int_{\Omega_{\mathbf{x},\epsilon}} q(x,r) \, r \, dx \, dr = 0 \right\}, \\
V(\Omega_{\mathbf{x},\epsilon}) &= \left\{ v \in H^1_r(\Omega_{\mathbf{x},\epsilon}) \ : \ v = 0 \text{ on } \Gamma_D^{AD} \right\},
\end{aligned} \tag{4}$$

with $\Gamma_D^{NS} = \Gamma_{w,\epsilon} \cup \Gamma_S$ and $\Gamma_D^{AD} = \Gamma_{in} \cup \Gamma_{w,\epsilon}$. The weak counterpart of problem (1) leads to find $c \in V(\Omega_{\mathbf{x},\epsilon})$, with $c = c_0$ on Γ_S, such that

$$a(c,v) + b(\mathbf{u};c,v) = 0 \qquad \forall v \in V_{\Gamma_S}(\Omega_{\mathbf{x},\epsilon}) \tag{5}$$

where $V_{\Gamma_S}(\Omega_{\mathbf{x},\epsilon}) = \left\{ v \in V(\Omega_{\mathbf{x},\epsilon}) : v = 0 \text{ on } \Gamma_S \right\}$,

$$a(c,v) = D \int_{\Omega_{\mathbf{x},\epsilon}} \nabla c \cdot \nabla v \, r \, dxdr, \qquad b(\mathbf{u};c,v) = \int_{\Omega_{\mathbf{x},\epsilon}} \mathbf{u} \cdot \nabla c \, v \, r \, dxdr. \tag{6}$$

Concerning the weak form of problem (2), we look for the pair $(\mathbf{u},p) = (u_x,u_r,p) \in W_x(\Omega_{\mathbf{x},\epsilon}) \times W_r(\Omega_{\mathbf{x},\epsilon}) \times Q(\Omega_{\mathbf{x},\epsilon})$, with $\mathbf{u} = \mathbf{f}$ on Γ_{in}, such that the following system of equations holds

$$\begin{cases} c_{NS}(\mathbf{u},\mathbf{u},\mathbf{w}) + a_{NS}(\mathbf{u},\mathbf{w}) + b_{NS}(p,\mathbf{w}) = 0 & \forall \mathbf{w} \in W_{x,\Gamma_{in}}(\Omega_{\mathbf{x},\epsilon}) \times W_{r,\Gamma_{in}}(\Omega_{\mathbf{x},\epsilon}) \\ b_{NS}(q,\mathbf{u}) = 0 & \forall q \in Q(\Omega_{\mathbf{x},\epsilon}), \end{cases} \tag{7}$$

with $W_{x,\Gamma_{in}}(\Omega_{\mathbf{x},\epsilon}) = \left\{ w_x \in W_x(\Omega_{\mathbf{x},\epsilon}) \ : \ w_x = 0 \text{ on } \Gamma_{in} \right\}$, $W_{r,\Gamma_{in}}(\Omega_{\mathbf{x},\epsilon}) = \left\{ w_r \in W_r(\Omega_{\mathbf{x},\epsilon}) \ : \ w_r = 0 \text{ on } \Gamma_{in} \right\}$, and where the trilinear and bilinear forms associated with the Navier-Stokes equations are

defined by

$$c_{NS}(\mathbf{v},\mathbf{u},\mathbf{w}) = \rho \int_{\Omega_{\mathbf{x},\epsilon}} (\mathbf{v}\cdot\nabla)\mathbf{u}\cdot\mathbf{w}\, r\, dx\, dr,$$

$$a_{NS}(\mathbf{u},\mathbf{w}) = 2\mu \int_{\Omega_{\mathbf{x},\epsilon}} \mathbf{E}(\mathbf{u}) \colon \mathbf{E}(\mathbf{w})\, r\, dx\, dr + 2\mu \int_{\Omega_{\mathbf{x},\epsilon}} \frac{1}{r}\, u_r\, w_r\, dx\, dr,$$

$$b_{NS}(q,\mathbf{w}) = -\int_{\Omega_{\mathbf{x},\epsilon}} (\partial_x w_x + \partial_r w_r)\; q\, r\, dx\, dr - \int_{\Omega_{\mathbf{x},\epsilon}} w_r\, q\, dx\, dr,$$

respectively. The approximation of problems (5) and (7) can be tackled using standard techniques, such as a finite element (FE) scheme. In line with the goal of the paper, we employ a HiMod discretization for the advection-diffusion problem, using a linear FE discretization on a sufficiently fine mesh as a reference to assess the effectiveness of the proposed approach. To compute the advective field $\mathbf{u}$ in (5), we solve the Navier-Stokes equations with the inf-sup stable FE pair $\mathbb{P}_2$-$\mathbb{P}_1$, used to approximate the velocity and pressure fields on a fine computational grid, respectively.

3 A fictitious domain formulation with HiMod reduction

In this section, we present the new combination of the FD approach with the HiMod formulation, for an efficient numerical simulation of advection-diffusion processes in stented vascular geometries. The following sections outline the mathematical formulation and the specific implementation issues related to merging the FD and HiMod methods, with a particular focus on the vascular application under consideration.

3.1 Fictitious domain formulation

The FD method extends the problem from a complex (in our specific case, the stented artery lumen) to a larger, more manageable domain, simplifying mesh generation and numerical treatment [31, 19, 5, 22, 32]. In particular, when boundary conditions have to be imposed on internal interfaces with intricate geometries – which are embedded in the extended domain and do not align with the computational mesh – standard techniques become impractical. In this setting, the Lagrange Multiplier (LM) approach provides an effective solution by allowing the weak imposition of such boundary conditions, enabling the use of non-conforming meshes while maintaining consistency and flexibility.

Thus, according to a FD formulation, the advection-diffusion equation (5) is solved in the extended domain $\Omega = \Omega_{\mathbf{x},\epsilon} \cup \omega_\epsilon$. The lumen-wall interface is now identified with Γ_w (see Figure 3), while the condition on Γ_S is enforced in a weak way through a LM. This requires a modification of the function spaces involved in (5), as both the drug concentration c and the test function v are now selected in $V(\Omega) = \{v \in H^1_r(\Omega) : v = 0 \text{ on } \Gamma_{in} \cup \Gamma_w\}$, whereas the boundary condition for c on Γ_S is no longer imposed in a strong fashion but enforced through a Lagrange multiplier.

Thus, the resulting FD formulation of equation (5) reads: find $c \in V(\Omega)$ and $\lambda \in (H^{\frac{1}{2}}(\Gamma_S))'$ such that

$$\begin{cases} a_\Omega(c,v) + b_\Omega(\mathbf{u};c,v) + \langle \lambda, v\rangle_{\Gamma_S} = 0 & \forall v \in V(\Omega) \\ \langle \mu, \mathrm{T}_{\Gamma_S} c\rangle_{\Gamma_S} = \langle \mu, c_0\rangle_{\Gamma_S} & \forall \mu \in (H^{\frac{1}{2}}(\Gamma_S))', \end{cases} \tag{8}$$

where μ is the test function associated with the LM, $\mathrm{T}_{\Gamma_S} : H^1_r(\Omega) \to H^{\frac{1}{2}}(\Gamma_S)$ is the trace operator that maps the concentration c, defined in the extended domain Ω, onto the boundary portion Γ_S, with $H^{\frac{1}{2}}(\Gamma_S)$ the space of traces of $H^1_r(\Omega)$-functions on Γ_S, symbol $\langle\cdot,\cdot\rangle_{\Gamma_S}$ denotes the duality pairing between $H^{\frac{1}{2}}(\Gamma_S)$ and its dual space $(H^{\frac{1}{2}}(\Gamma_S))'$, while the bilinear forms $a_\Omega(\cdot,\cdot)$, $b_\Omega(\mathbf{u};\cdot,\cdot)$ extend definitions in (6) to the entire domain Ω. We observe that the second equation in (8) imposes the boundary data for c on Γ_S, while the term $\langle \lambda, v\rangle_{\Gamma_S}$ in the first equation corresponds to the normal

flux jump, $D\nabla c \cdot \mathbf{n}$, of c across Γ_S, being $\lambda = -D(\nabla c \cdot \mathbf{n}^+ + \nabla c \cdot \mathbf{n}^-)$, with $\mathbf{n}^\pm$ the outward unit normal vectors to Γ_S [1].
Note that, with an abuse of notation, we denote by $\mathbf{u}$ in (8) the constant extension of the advective field $\mathbf{u}$, originally defined in $\Omega_{\mathbf{x},\epsilon}$ through the solution of (7), to the whole Ω. In practice, we extend $\mathbf{u}$ by defining a null advection inside ω_ϵ, thus ensuring continuity across the entire computational domain. This guarantees that the influence of the advective field is consistent throughout the extended domain, while maintaining the original physical conditions in the perforated region.

3.1.1 Reduced interface conditions

The primary idea of this reduced modeling approach is to enforce the boundary condition on Γ_S in a simplified manner through a low-dimensional approximation, $F_{N_{LM}}$, of the infinite-dimensional trace space $H^{\frac{1}{2}}(\Gamma_S)$.
Considering the partition, $\Gamma_{LM} = \{\Gamma_{i_{LM}}\}_{i_{LM}=1}^{N_{LM}}$, of the boundary Γ_S, such that

$$\overline{\Gamma}_S = \bigcup_{i_{LM}=1}^{N_{LM}} \Gamma_{i_{LM}}, \quad \mathring{\Gamma}_{i_{LM}} \cap \mathring{\Gamma}_{j_{LM}} = \emptyset \qquad \forall\, i_{LM} \neq j_{LM},$$

the space $F_{N_{LM}}$ can be defined as

$$F_{N_{LM}} = \Big\{ v \in L^2(\Gamma_S) \,:\, v\big|_{\Gamma_{i_{LM}}} = v_{i_{LM}} \in \mathbb{R}, \;\; \text{for} \;\; i_{LM} = 1, \dots, N_{LM} \Big\}. \tag{9}$$

Space $F_{N_{LM}}$ coincides with the set of piecewise constant functions associated with the partition Γ_{LM} of Γ_S. For the purposes of this work, we restrict our analysis to low-dimensional cases, i.e., we choose $N_{LM} = 1, 2, 3$. In Figure 4 we show some examples of the partition Γ_{LM} for the lumen-stent interface, corresponding to $N_{LM} = 1, 2, 3$. In particular, for $N_{LM} = 3$, we consider two alternative subdivisions of Γ_S: option (c) is devised to prevent any coupling among the stent faces, whereas option (d) is intended to explicitly account for such an interaction. This consideration will be particularly useful to manage the case of a zero flux condition across $\Gamma_{w,\epsilon}$ (namely, of a null flux condition across Γ_w) as shown in Section 4.1.2 (see Figure 16).
Therefore, the definition of the space $F_{N_{LM}}$ allows us to reformulate problem (8) as the following reduced advection-diffusion problem: find $c \in V(\Omega)$ and $\lambda_{N_{LM}} \in F_{N_{LM}}$ such that:

$$\begin{cases} a_\Omega(c, v) + b_\Omega(\mathbf{u}; c, v) + (\lambda_{N_{LM}}, v)_{\Gamma_S} = 0 & \forall v \in V(\Omega) \\ (\mu_{N_{LM}}, \mathrm{T}_{\Gamma_S} c)_{\Gamma_S} = (\mu_{N_{LM}}, c_0)_{\Gamma_S} & \forall \mu_{N_{LM}} \in F_{N_{LM}}, \end{cases} \tag{10}$$

where $(f, g)_{\Gamma_S} = \int_{\Gamma_S} f(x, r) g(x, r) r \, dx dr$ denotes the surface integral in cylindrical coordinates. Note that using the reduced space $F_{N_{LM}}$ to approximate the trace space yields a discretized formulation with substantially fewer degrees of freedom associated with the Lagrange multiplier. This strategy has already proven particularly effective in settings that demand high computational efficiency and involve small obstacles, while maintaining accuracy [25, 5, 32].

The discrete counterpart of the advection-diffusion reduced model (10), obtained via a FE scheme, is denoted in the following as reduced FD-FEM. In particular, we adopt a linear FE discretization to approximate the concentration c.

[1] Splitting the diffusion term $a_\Omega(c, v)$ in (8) on the perforated domain $\Omega_{\mathbf{x},\epsilon}$ and on the obstacle ω_ϵ, integrating both terms by parts, and exploiting the extension of (1) to the whole Ω so that $D\Delta c = \mathbf{u} \cdot \nabla c$ in Ω, it follows [5]

$$\begin{aligned} a_\Omega(c, v) &= D(\nabla c, \nabla v)_{\Omega_{\mathbf{x},\epsilon}} + D(\nabla c, \nabla v)_{\omega_\epsilon} = -D(\Delta c, v)_\Omega + (D(\nabla c \cdot \mathbf{n}^+ + \nabla c \cdot \mathbf{n}^-), v)_{\Gamma_S} \\ &= -(\mathbf{u} \cdot \nabla c, v)_\Omega - \langle \lambda, v \rangle_{\Gamma_S} = -b_\Omega(\mathbf{u}; c, v) - \langle \lambda, v \rangle_{\Gamma_S}. \end{aligned}$$

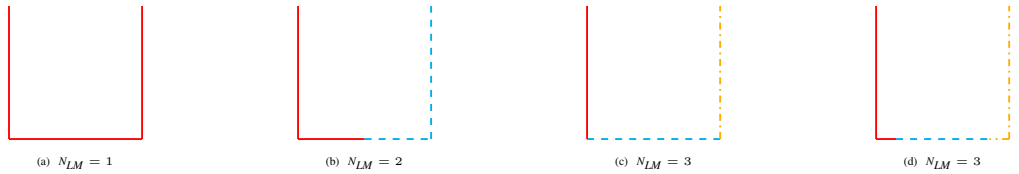

Figure 4: Examples of partition Γ_{LM} of the lumen-stent interface Γ_S for different values of N_{LM}.

3.2 Hierarchical model reduction with fictitious domains

In this section, we apply the HiMod reduction [14, 45] to the advection-diffusion problem in (10). A HiMod discretization begins with the assumption that the computational domain can be represented as a fiber bundle, $\Omega = \bigcup_{x\in\Omega_{1D}}\{x\} \times \gamma_x$, where $\Omega_{1D} = (0, L)$ is a one-dimensional supporting fiber aligned with the main dynamics of the phenomenon under study, while $\gamma_x \subset \mathbb{R}$ denotes the transverse fiber at $x \in \Omega_{1D}$, orthogonal to Ω_{1D} and aligned with the secondary dynamics. In the axisymmetric context considered in this paper, the leading direction is identified by the coordinate x, which changes along Γ_{axi} and thus coincides with Ω_{1D}, while γ_x corresponds to the domain over which the radial coordinate r varies. Moreover, since the fiber γ_x is independent of x, all transverse fibers are identical and are denoted simply by $\gamma = (0, R)$ (see the sketch in Figure 3).

A HiMod reduction relies on the introduction of a map $\Psi : \Omega \to \hat{\Omega}$, which transforms the physical domain Ω into a reference simpler domain $\hat{\Omega}$, so that $\Psi(\mathbf{x}) = \Psi(x, r) = \hat{\mathbf{x}} = (\hat{x}, \hat{r})$, for any $(x, r) \in \Omega$ [45]. The idea is to carry out all computations in the simplified domain $\hat{\Omega}$ and then map the results to different computational domains under the action of the inverse of map Ψ. It is worth noting that HiMod reduction requires the map Ψ, as well as its inverse, to satisfy specific regularity assumptions such as differentiability (see, e.g., the paper [45] for detailed requirements). These conditions exclude irregular profiles, such as those induced by the presence of a stent. This, in turn, justifies the adoption of the FD method, which allows HiMod to be applied to configurations with irregular geometries such as stented arteries, otherwise disregarded in the conventional HiMod theory. In particular, since the domain underlying the FD approach coincides with a very simple geometry (i.e., a rectangle), we can directly identify the reference domain $\hat{\Omega}$ with the fictitious domain Ω. This allows us to avoid the use of the map Ψ in the formalization of the HiMod methodology, significantly simplifying both the theoretical treatment and the numerical computations.

The separation of variables paradigm underlying a HiMod formulation allows the construction of the reduced HiMod space by combining functional settings associated with the leading and the transverse direction, respectively. In more detail, we associate the space $V_{1D} \subseteq H^1(\Omega_{1D})$ with the supporting fiber and the set $\{\phi_k\}_{k\in\mathbb{N}^+} \subset H^1_r(\gamma)$ of modal basis functions with γ.
Following the seminal paper [45], we identify V_{1D} with the space of the continuous FE functions corresponding to a partition $\mathcal{T}_h$ of Ω_{1D}. In particular, we choose linear FE for the discretization in the leading direction. Notice that the FE basis, denoted by $\{\theta_l\}_{l=1}^{N_h}$, must be compatible with the possible imposition of essential boundary conditions on Γ_{in} and Γ_{out}. As for the modal basis, the functions ϕ_k are assumed to be orthonormal with respect to the $L^2_r(\gamma)$-product, so that

$$\int_\gamma \phi_k(r)\phi_l(r) r\, dr = \delta_{kl} \qquad \forall\, k, l \ \in \mathbb{N}^+ \tag{11}$$

with δ_{kl} the Kronecker symbol[2]. Functions ϕ_k are designed to accommodate the boundary conditions prescribed on the horizontal sides, Γ_w and Γ_{axi}, of the domain Ω. In a previous work [1], the authors propose a practical method to construct such functions, by solving an auxiliary Sturm-Liouville eigenvalue problem which enforces the desired boundary data in an essential manner, regardless

[2]It can be verified that $(f, g)_\gamma = \int_\gamma f(r)g(r)r\, dr$ defines an inner product on the weighted space $L^2_r(\gamma)$ when f and g belong to the classical space $L^2(\gamma)$.

of the specific type. In particular, the resulting eigenfunctions constitute the modal basis $\{\phi_k\}$. Concerning the specific application in Section 4, we adopt a more pragmatic approach by selecting ad-hoc basis functions that directly satisfy the boundary conditions on Γ_w and Γ_{axi} (see Sections 4.1.1 and 4.1.2 for more details). Then, these functions are post-processed using a Gram-Schmidt orthonormalization procedure to ensure property (11).

Thus, the HiMod approximation of problem (10) can be formulated as: find $c \in V_M$ and $\lambda_{N_{LM}} \in F_{N_{LM}}$ such that

$$\begin{cases} a_\Omega(c,v) + b_\Omega(\mathbf{u};c,v) + (\lambda_{N_{LM}}, v)_{\Gamma_S} = 0 & \forall v \in V_M \\ (\mu_{N_{LM}}, \mathrm{T}_{\Gamma_S} c)_{\Gamma_S} = (\mu_{N_{LM}}, c_0)_{\Gamma_S} & \forall \mu_{N_{LM}} \in F_{N_{LM}}, \end{cases} \tag{12}$$

where

$$V_M = \left\{ v(\mathbf{x}) = \sum_{k=1}^{M} \tilde{v}_k(x)\phi_k(r) \,:\, \tilde{v}_k \in V_{1D} \text{ with } \mathbf{x} = (x,r) \in \Omega \right\} \tag{13}$$

denotes the HiMod space. The modal index M, defining the level of detail of the reduced model, can be chosen a priori from knowledge of the phenomenon under investigation, rather than automatically determined through an a posteriori modeling error analysis (we refer the interested reader to previous studies [46, 42]).

3.2.1 Algebraic representation

In this section we derive the algebraic representation of the HiMod formulation in (12). To this aim, we expand the HiMod solution c and the generic HiMod test function v in terms of the modal and FE basis functions, namely

$$c(\mathbf{x}) = \sum_{j=1}^{M}\sum_{i=1}^{N_h} \theta_i(x)\phi_j(r)c_{ij}, \quad v(\mathbf{x}) = \theta_l(x)\phi_k(r) \tag{14}$$

for $k = 1,\dots,M$, $l = 1,\dots,N_h$, so that the actual unknowns of formulation (12) are the MN_h coefficients $c_{ij} \in \mathbb{R}$, with $j = 1,\dots,M$, $i = 1,\dots,N_h$, in addition to the N_{LM} coefficients defining the Lagrange multiplier $\lambda_{N_{LM}}$.

Now, we exploit expansions (14) in the definition of the bilinear forms in $(12)_1$, thus obtaining

$$\begin{aligned} & a_\Omega(c,v) = D\int_\Omega \nabla c(\mathbf{x})\cdot\nabla v(\mathbf{x})\, r\, dxdr \\ = & \sum_{j=1}^{M}\sum_{i=1}^{N_h} c_{ij}\, D \int_\Omega \left[(\phi_j\phi_k)\,\theta_i'\theta_l' + \left(\phi_j'\phi_k'\right)\theta_i\theta_l \right] r\, dxdr, \end{aligned} \tag{15}$$

$$\begin{aligned} & b_\Omega(\mathbf{u};c,v) = \int_\Omega \mathbf{u}(\mathbf{x})\cdot\nabla c(\mathbf{x}) v(\mathbf{x})\, r\, dxdr \\ = & \sum_{j=1}^{M}\sum_{i=1}^{N_h} c_{ij} \int_\Omega \left[(u_x(\mathbf{x})\phi_j\phi_k)\,\theta_i'\theta_l + \left(u_r(\mathbf{x})\phi_j'\phi_k\right)\theta_i\theta_l \right] r\, dxdr, \end{aligned} \tag{16}$$

respectively where the dependence of functions θ_i (θ_l) on x and of functions ϕ_j (ϕ_k) on r is here left implicit. Thus, by collecting the corresponding terms from (15) and (16) and exploiting the separation of variables underlying the HiMod formulation, we obtain

$$a_\Omega(c,v) + b_\Omega(\mathbf{u};c,v) = \sum_{j=1}^{M}\sum_{i=1}^{N_h} \mathcal{A}_{jk}(\theta_i,\theta_l)c_{ij}, \tag{17}$$

being $v = \theta_l \phi_k$ for $k = 1, \dots, M$, $l = 1, \dots, N_h$, and where

$$\mathcal{A}_{jk}(\theta_i, \theta_l) = \int_{\Omega_{1D}} \left[\mathcal{Q}_{jk}^{11}\, \theta_i'(x)\theta_l'(x) + \mathcal{Q}_{jk}^{10}(x)\, \theta_i'(x)\theta_l(x) + \mathcal{Q}_{jk}^{00}(x)\, \theta_i(x)\theta_l(x) \right] dx. \tag{18}$$

In particular, coefficients $\mathcal{Q}_{jk}^{st}$, with $s, t = 0, 1$, depend explicitly on the problem data and on the chosen modal basis, and account for the dynamics in the radial direction, being defined as

$$\begin{aligned} \mathcal{Q}_{jk}^{11} = D \int_\gamma \phi_j(r)\phi_k(r) r\, dr, \quad \mathcal{Q}_{jk}^{10}(x) = \int_\gamma u_x(x,r)\phi_j(r)\phi_k(r) r\, dr, \\ \mathcal{Q}_{jk}^{00}(x) = \int_\gamma \left[D\, \phi_k'(r) + u_r(x,r)\phi_k(r) \right] \phi_j'(r) r\, dr. \end{aligned} \tag{19}$$

We now consider the term in $(12)_1$ associated with the boundary portion Γ_S. To properly define it, the partition $\mathcal{T}_h$ along Ω_{1D} has to be consistent with the obstacle geometry, meaning that the vertical sides of the obstacle must correspond in the x-direction to specific vertices of $\mathcal{T}_h$, here denoted by x_{l_1} and x_{l_2}, respectively. Based on the modal representation $v = \theta_l \phi_k$ in (14) and the definition of the space $F_{N_{LM}}$ in (9), we have

$$(\lambda_{N_{LM}}, v)_{\Gamma_S} = \int_{\Gamma_S} \lambda_{N_{LM}} v(x,r) r\, dx dr = \sum_{i_{LM}=1}^{N_{LM}} \lambda_{i_{LM}} \int_{\Gamma_{i_{LM}}} \theta_l(x)\phi_k(r) r\, dx dr \tag{20}$$

for $k = 1, \dots, M$, $l = 1, \dots, N_h$. To streamline the derivation, we expand the computations in the simplified case of a single Lagrange multiplier, that is, we set $N_{LM} = 1$ in (20) and denote λ_1 simply by λ, thus obtaining

$$(\lambda, v)_{\Gamma_S} = \lambda \int_{\Gamma_S} \theta_l(x)\phi_k(r) r\, dx dr = \mathcal{A}_k^{LM}(\theta_l)\, \lambda \tag{21}$$

for $k = 1, \dots, M$, with

$$\mathcal{A}_k^{LM}(\theta_l) = \left[\theta_l(x_{l_1}) \int_{\bar{r}}^{R} \phi_k(r) r\, dr + \phi_k(\bar{r})\, \bar{r} \int_{x_{l_1}}^{x_{l_2}} \theta_l(x)\, dx + \theta_l(x_{l_2}) \int_{\bar{r}}^{R} \phi_k(r) r\, dr \right] \tag{22}$$

and $\bar{r}$ the distance of the stent bottom edge from Γ_{axi}. The first and third integrals are associated with the vertical sides of Γ_S and provide a contribution only to the FE basis functions θ_{l_1} and θ_{l_2}. The second integral, instead, is associated with the horizontal side of the stent and therefore contributes to all basis functions θ_l with $l \in \{l_1, \dots, l_2\}$.

With regard to equation $(12)_2$, we first introduce a HiMod expansion for the trace term $\mathrm{T}_{\Gamma_S} c$, which can be rewritten as

$$\mathrm{T}_{\Gamma_S} c(\mathbf{x}) = \sum_{j=1}^{M} \sum_{i=l_1}^{l_2} \theta_i(x)\phi_j(r) c_{ij} \quad \text{for } r \in (\bar{r}, R). \tag{23}$$

Thus, the boundary contribution $(\mu_{N_{LM}}, \mathrm{T}_{\Gamma_S} c)_{\Gamma_S}$ takes the form

$$\int_{\Gamma_S} \mu_{N_{LM}}\, \mathrm{T}_{\Gamma_S} c(x,r) r\, dx dr = \sum_{i_{LM}=1}^{N_{LM}} \mu_{i_{LM}} \left[\sum_{j=1}^{M} \sum_{i=l_1}^{l_2} c_{ij} \int_{\Gamma_{i_{LM}}} \theta_i(x)\phi_j(r) r\, dx dr \right], \tag{24}$$

which, after setting $N_{LM} = 1$ and $\mu_1 = \mu$, simplifies to

$$\int_{\Gamma_S} \mu_{N_{LM}}\, \mathrm{T}_{\Gamma_S} c(x,r) r\, dx dr = \mu \sum_{j=1}^{M} \sum_{i=l_1}^{l_2} c_{ij} \int_{\Gamma_S} \theta_i(x)\phi_j(r) r\, dx dr = \mu \sum_{j=1}^{M} \sum_{i=l_1}^{l_2} \mathcal{A}_j^{LM}(\theta_i) c_{ij}, \tag{25}$$

with

$$\mathcal{A}_j^{LM}(\theta_i) = \left[\theta_i(x_{l_1}) \int_{\bar{r}}^{R} \phi_j(r) r \, dr + \phi_j(\bar{r})\, \bar{r} \int_{x_{l_1}}^{x_{l_2}} \theta_i(x)\, dx + \theta_i(x_{l_2}) \int_{\bar{r}}^{R} \phi_j(r) r \, dr\right],$$

consistently with (22). Concerning the right-hand side in $(12)_2$, it simplifies to

$$(\mu, c_0)_{\Gamma_S} = \mu c_0 \int_{\Gamma_S} r \, dxdr = \mu c_0 \, |\Gamma_S| = \mu \mathcal{B}^{LM}$$

with $\mathcal{B}^{LM} = c_0 \, |\Gamma_S|$, $|\Gamma_S|$ denoting the measure of the stent surface[3].

Thus, to provide the algebraic counterpart of problem (12), we first rearrange the coefficients c_{ij} in (14) into a vector $\mathbf{c} \in \mathbb{R}^{MN_h}$, ordered by FE node (for a fixed mode) and subsequently by mode,

$$\mathbf{c} = [\mathbf{c}_1, \mathbf{c}_2, \ldots, \mathbf{c}_M]^T \quad \text{with} \quad \mathbf{c}_k = [c_{1k}, c_{2k}, \ldots, c_{N_h k}]^T \in \mathbb{R}^{N_h} \quad k = 1, \ldots, M.$$

Then, we associate: a matrix $A_{jk} \in \mathbb{R}^{N_h \times N_h}$ with coefficients $\mathcal{A}_{jk}$ in (18), being

$$[A_{jk}]_{li} = \mathcal{A}_{jk}(\theta_i, \theta_l) \quad i, l = 1, \ldots, N_h, \quad j, k = 1, \ldots, M;$$

a vector $A_k^{LM} \in \mathbb{R}^{N_h}$ with quantities $\mathcal{A}_k^{LM}$ in (22), such that

$$[A_k^{LM}]_l = \mathcal{A}_k^{LM}(\theta_l) \quad l = 1, \ldots, N_h, \quad k = 1, \ldots, M.$$

These notations allow us to rewrite the HiMod formulation (12), when employing a single LM, as the following system of linear equations

$$\begin{bmatrix} A & A^{LM} \\ [A^{LM}]^T & 0 \end{bmatrix} \begin{bmatrix} \mathbf{c} \\ \lambda \end{bmatrix} = \begin{bmatrix} A_{11} & \cdots & A_{M1} & A_1^{LM} \\ \vdots & \ddots & \vdots & \vdots \\ A_{1M} & \cdots & A_{MM} & A_M^{LM} \\ [A_1^{LM}]^T & \cdots & [A_M^{LM}]^T & 0 \end{bmatrix} \begin{bmatrix} \mathbf{c}_1 \\ \vdots \\ \mathbf{c}_M \\ \lambda \end{bmatrix} = \begin{bmatrix} \mathbf{0} \\ \vdots \\ \mathbf{0} \\ \mathcal{B}^{LM} \end{bmatrix}. \tag{26}$$

The solution of the HiMod system (26) is denoted as FD-HiMod in the following. Specifically, the leading dynamics is discretized with linear FE, while the transverse behavior is modeled through modal functions tailored to the boundary data prescribed on Γ_w.

The sparsity pattern of the FD-HiMod system matrix is shown in Figure 5 for a representative case with 1 LM, 200 intervals in Ω_{1D}, and 5 modes. The main contribution in A (in red) exhibits the characteristic block structure of the HiMod approach, with 5×5 blocks. Each block has the typical tridiagonal pattern of the linear FE basis (see the gray square). The contributions from the LM in $[A^{LM}]^T$ and the weakly imposed boundary conditions on Γ_S in A^{LM} are added as one additional row and column (in blue), respectively. These contributions also display a repeated block pattern, consistently with the previously chosen value of $M = 5$. Within each block, non-zero entries appear only at the nodes indexed by $l \in \{l_1, \ldots, l_2\}$ (see the yellow circle). For a single LM, two out of the 200 intervals of Ω_{1D} are involved, corresponding to three nodes with non-zero entries per block.

4 Numerical simulation of drug release

In this section, we present numerical results for drug release in vascular stented configurations using the proposed FD-HiMod method. The purpose of the simulations is to validate this new methodology

[3]The area of the annular recess occupied by the stent is obtained by summing the area of the two annular regions defined by concentric circles of radius R and $\bar{r}$, respectively (i.e., $2\pi(R^2 - \bar{r}^2)$), with the area of the lateral surface of a cylinder of radius $\bar{r}$ and height $(x_{l_2} - x_{l_1})$ (i.e., $2\pi\bar{r}(x_{l_2} - x_{l_1})$), so that $\int_{\hat{\Gamma}_S} d\hat{S} = 2\pi[R^2 - \bar{r}^2 + \bar{r}(x_{l_2} - x_{l_1})]$. Now, exploiting the relation between the integrals on $\hat{\Gamma}_S$ and Γ_S, it follows $\int_{\Gamma_S} r \, dxdr = R^2 - \bar{r}^2 + \bar{r}(x_{l_2} - x_{l_1})$.

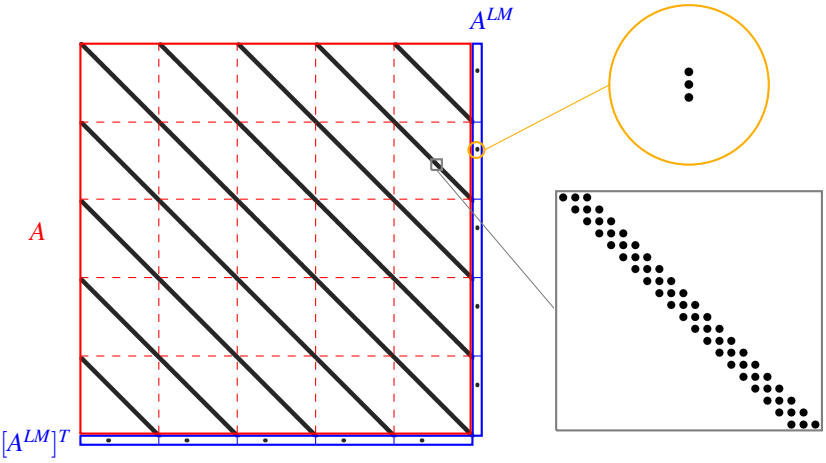

Figure 5: Sparsity pattern of the FD-HiMod system matrix for $N_{LM} = 1$: the red square highlights the classical HiMod matrix A, with block structure indicated by red dashed lines. Each block shows a tridiagonal pattern typical of linear FE discretization (grey square). The blue rectangles indicate the contributions from the FD approach, A^{LM} and $[A^{\mathrm{LM}}]^T$, with their block structure and a focus on the non-zero entries (yellow circle).

and to assess its accuracy and efficiency against the reduced FD-FEM approach, when using finite elements on both conforming and non-conforming grids. The numerical simulations are divided into two main categories:

1. a benchmark case designed to evaluate the performance of the FD-HiMod approximation on simple configurations with a well-defined reference solution;

2. a production case, focusing on a more realistic configuration and highlighting the practical applicability of the proposed approach in clinical settings through a sensitivity analysis of ring spacing.

From a modeling viewpoint, we assume that the concentration is normalized with respect to the initial drug load, c_0, thus becoming dimensionless. Moreover, for simplicity, the spatial units of the coordinates x and r, the mesh size h (either in the reduced FD-FEM or along the HiMod supporting fiber Ω_{1D}), and the ring spacings are omitted, with all quantities expressed in millimeters (mm). Finally, the reduced FD-FEM results, as well as all reference solutions used in this work, are obtained using the open-source software FreeFEM, while the FD-HiMod approach is implemented in MATLAB[4].

4.1 The benchmark case

The final objective of this section is to assess the discrepancy between the reduced FD-FEM and the FD-HiMod approaches with respect to a high-fidelity solution, providing insights into the effectiveness of the proposed method and the potential applicability to realistic configurations, such as the one considered in Section 4.2.

Here, we consider a simplified stent model, consisting of a single-ring structure embedded in a circular lumen. The solution is computed under a constant advective field, $\mathbf{u} = (1, 0)^T$, ensuring

[4]The simulations are performed on a laptop with a 2,3 GHz Quad-Core Intel ®Core™i5 processor, integrated with Intel ®Iris Plus Graphics, and 16 GB of RAM.

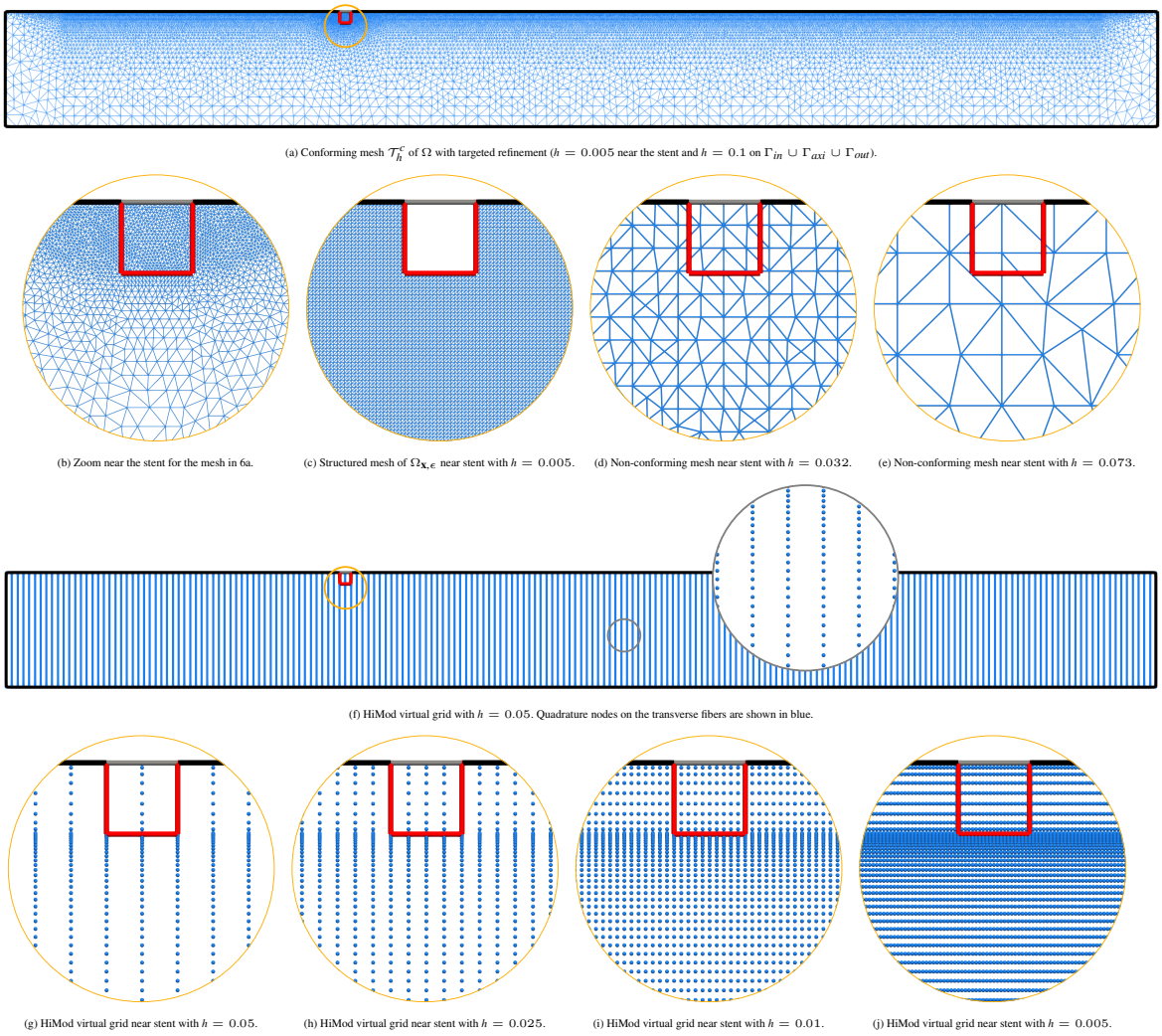

(a) Conforming mesh $\mathcal{T}_h^c$ of Ω with targeted refinement ($h = 0.005$ near the stent and $h = 0.1$ on $\Gamma_{in} \cup \Gamma_{axi} \cup \Gamma_{out}$).

(b) Zoom near the stent for the mesh in 6a.

(c) Structured mesh of $\Omega_{\mathbf{x},\epsilon}$ near stent with $h = 0.005$.

(d) Non-conforming mesh near stent with $h = 0.032$.

(e) Non-conforming mesh near stent with $h = 0.073$.

(f) HiMod virtual grid with $h = 0.05$. Quadrature nodes on the transverse fibers are shown in blue.

(g) HiMod virtual grid near stent with $h = 0.05$.

(h) HiMod virtual grid near stent with $h = 0.025$.

(i) HiMod virtual grid near stent with $h = 0.01$.

(j) HiMod virtual grid near stent with $h = 0.005$.

Figure 6: Benchmark case: reduced FD-FEM and FD-HiMod grids, for different choices of the mesh size h.

that the global Péclet number remains strictly below one. Specifically, the advective field is extended as constant throughout the FD domain Ω, so that the condition $\mathbf{u} = (1, 0)^T$ also holds inside the obstacle ω_ϵ. This choice avoids potential errors that would arise if $\mathbf{u}$ were taken from the Navier-Stokes solution in (2).

We exploit this simple setup to compare the accuracy of the reduced FD-FEM and of the FD-HiMod approaches under various settings, including mesh type, LM arrangement, and boundary conditions on the artery wall Γ_w.

Regarding the mesh, we distinguish between conforming and non-conforming grids for the reduced FD-FEM approximation (see Figure 6). In the conforming case, we consider a targeted refined mesh, $\mathcal{T}_h^c$, where $h = 0.005$ near the stent and $h = 0.1$ on $\Gamma_{in} \cup \Gamma_{axi} \cup \Gamma_{out}$, yielding a mesh approximately consisting of 46,500 triangles (see Figures 6a and 6b). In the non-conforming case, the mesh size is chosen uniform, so as to avoid nodes coinciding with the stent boundary Γ_S (see Figures 6d and 6e). As for the FD-HiMod approach, no actual mesh of the full computational domain is constructed, since the HiMod formulation only requires discretization along the supporting fiber, to which we

associate the mesh size h. Nevertheless, in the r-direction it is computationally convenient to refer to the quadrature nodes used for evaluating the integrals involved in (12). The set of these nodes constitutes the so-called virtual grid. In particular, the quadrature nodes are selected to conform to the obstacle geometry and to guarantee sufficient accuracy in the integral evaluation for a reasonably large number M of modes (see Figures 6f-6j, which illustrate the virtual grid for different mesh sizes h, i.e., for a diverse spacing of the HiMod fibers).
Concerning the LM arrangement, we analyze cases with one, two, or three LMs according to the different options illustrated in Figure 4.
Finally, the boundary Γ_w is treated as a perfect sink in Section 4.1.1, in contrast to Section 4.1.2, where it is modeled as a membrane in equilibrium with zero flux.

In the next sections, the accuracy of the reduced FD-FEM and FD-HiMod solutions is assessed against a high-fidelity linear FE approximation. This is computed on a conforming mesh of the perforated domain $\Omega_{\mathbf{x},\epsilon}$, obtained from the mesh of Ω in Figure 6a by removing the obstacle ω_ϵ, delimited by the red boundary Γ_S where the Dirichlet boundary condition $c = c_0$ in (1) is strongly enforced. The high-fidelity solution is then interpolated onto the structured triangular mesh in Figure 6c, yielding the reference solution c_R used throughout the analysis below. The projection step ensures a fair comparison of c_R with the reduced FD-FEM and FD-HiMod solutions. Both the approximations are linearly interpolated onto the same structured mesh, thus avoiding additional errors that would arise from projecting HiMod results onto an unstructured FE mesh.

Accuracy is examined with respect to the mesh size h for both reduced FD-FEM and FD-HiMod approximations, and with respect to the number M of modes for FD-HiMod only. We will also investigate the impact of the total number of degrees of freedom (#DOFs) on accuracy, where

$$\#\text{DOFs(reduced FD-FEM)} = N_h + N_{LM}, \ \#\text{DOFs(FD-HiMod)} = N_h M + N_{LM}. \tag{27}$$

The control parameter in the reduced FD-FEM is the mesh size h (i.e., the number of mesh nodes N_h) together with the number, N_{LM}, of Lagrange multipliers, while in FD-HiMod the number, M, of modes also contributes.

4.1.1 Perfect Sink Boundary Conditions

In this section we treat the artery wall as a perfect sink, which is equivalent to imposing homogeneous Dirichlet boundary conditions on Γ_w. Accordingly, we select the modal basis functions in the HiMod expansion (14) as

$$\phi_k(r) = \cos\left(\left(\pi k - \frac{\pi}{2}\right) r\right) \quad k = 1, \dots, M.$$

For this configuration, we analyze the performance of the reduced FD-FEM and FD-HiMod approaches as the number of LMs, the mesh size, and the number M of modal functions ϕ_k vary.
Figure 7 shows the color plot of the reference solution, c_R. As a first validation, Figure 8 shows the comparison between c_R, the reduced FD-FEM approximation (with both conforming and non-conforming meshes), and the FD-HiMod discretization, along the white section highlighted in Figure 7. In more detail, the conforming reduced FD-FEM solution is computed on the mesh shown in Figures 6a-6b, the non-conforming reduced FD-FEM model relies on a mesh similar to those in Figures 6d-6e with $h = 0.043$, while for the FD-HiMod approximation we set $h = 0.05$ along the supporting fiber and choose $M = 30$. This corresponds to approximately 23,000 DOFs for the conforming reduced FD-FEM and about 6,000 DOFs for both the non-conforming reduced FD-FEM and the FD-HiMod approximation. The number of LMs is varied in all cases. In particular, for $N_{LM} = 3$, we adopt the configuration shown in Figure 4c.
All reduced solutions underestimate the concentration near the stent and produce local overshoots and undershoots. For all the models, accuracy improves with two or three LMs, particularly in capturing the downstream decay. Overall, the FD-HiMod outperforms the non-conforming reduced FD-FEM, for a comparable number of degrees of freedom, provided that the mesh size and number

of modes are appropriately chosen. The conforming reduced FD-FEM model, on the other hand, is slightly more accurate than FD-HiMod, but this comes at the cost of a significantly higher number of DOFs.

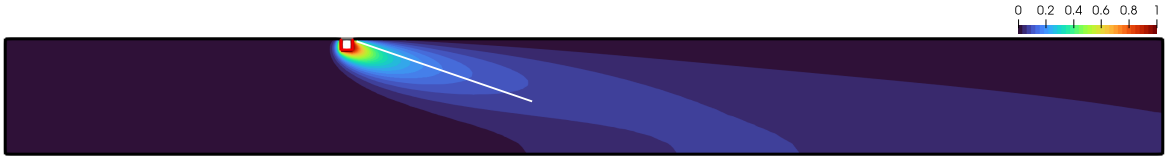

Figure 7: Benchmark case (perfect sink boundary conditions): reference solution. The white line marks the section selected for the analysis in Figure 8.

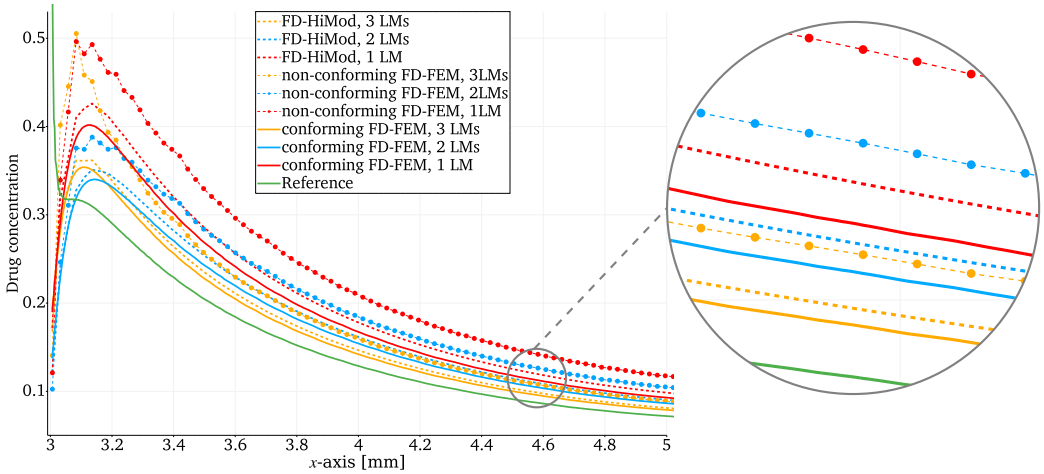

Figure 8: Benchmark case (perfect sink boundary conditions): comparison of drug distribution along the section highlighted in Figure 7 among the reference solution (solid green line), the conforming (dashed lines) and the non-conforming (dotted lines) reduced FD-FEM, and the FD-HiMod (solid lines) approximation for a different number of LMs.

We now qualitatively analyze the pointwise distribution of the signed error between the reference solution c_R, the conforming/non-conforming reduced FD-FEM approximation and the FD-HiMod discretization. The pointwise error is primarily concentrated near the stent, so we focus the comparison in this region (see Figure 9). We distinguish regions where the reduced FD-FEM and the FD-HiMod solutions underestimate (positive values) or overestimate (negative values) the reference concentration. The conforming reduced FD-FEM scheme provides a baseline, with most error arising from the weak enforcement of Dirichlet conditions on Γ_S in combination with the reduced LM approach presented in (10). Increasing the number of LMs localizes the error closer to the stent but also introduces more alternating positive and negative values. The non-conforming reduced FD-FEM error exhibits a similar pattern, but more spread and with higher peaks. Finally, with the FD-HiMod approximation, both the magnitude and spatial extent of the error decrease as the number of modes M increases. A sufficient number of modes is required to prevent oscillations from propagating from the stent toward $r = 0$, a characteristic inherent to the trigonometric modal expansion. Moreover, with higher LM counts, the error alternations may intensify if the number of modes is not large enough, producing larger peak oscillations, as observed when comparing the case with 3 LMs to the choice of 1 LM for $M = 10$.

To quantify the discrepancy between the reference and the reduced FD-FEM and FD-HiMod

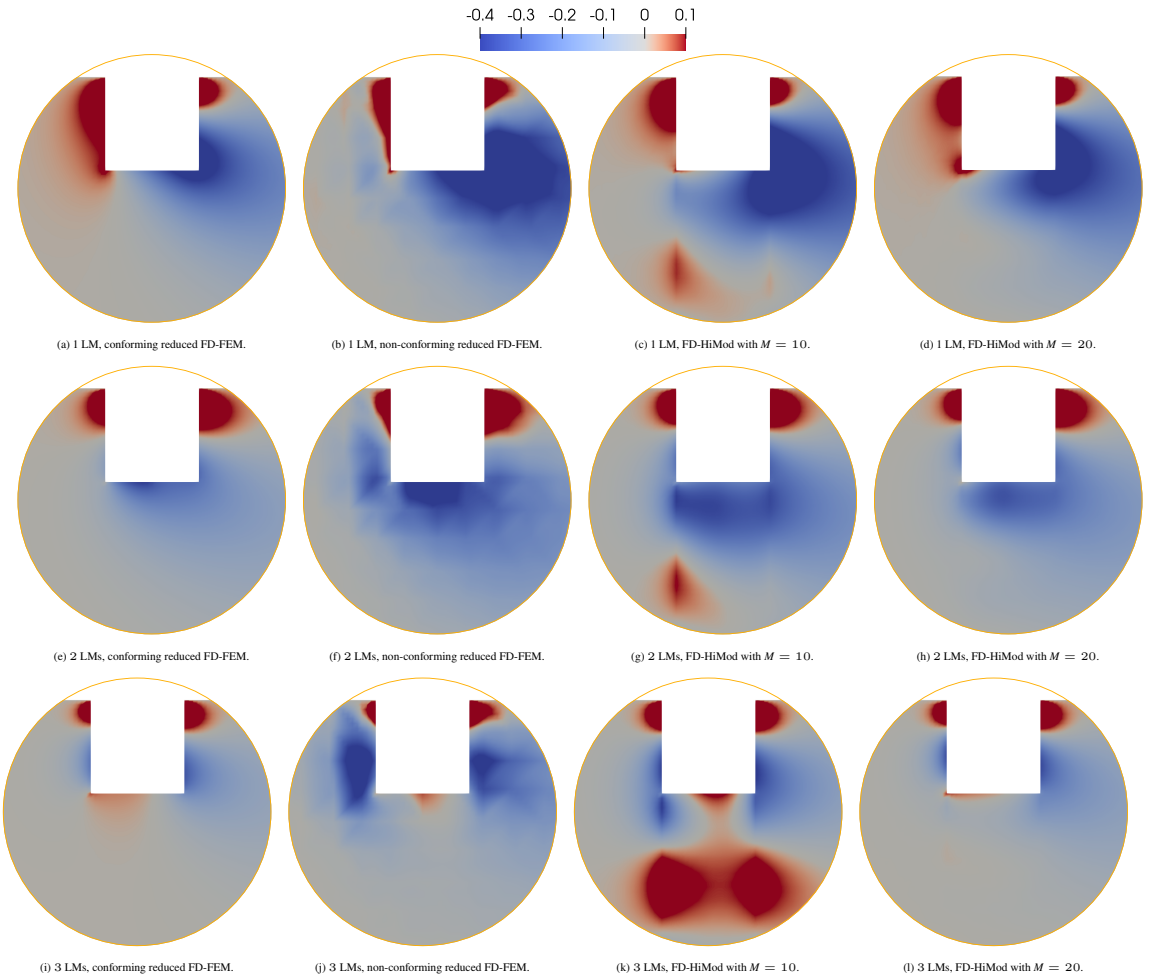

(a) 1 LM, conforming reduced FD-FEM. (b) 1 LM, non-conforming reduced FD-FEM. (c) 1 LM, FD-HiMod with $M = 10$. (d) 1 LM, FD-HiMod with $M = 20$.

(e) 2 LMs, conforming reduced FD-FEM. (f) 2 LMs, non-conforming reduced FD-FEM. (g) 2 LMs, FD-HiMod with $M = 10$. (h) 2 LMs, FD-HiMod with $M = 20$.

(i) 3 LMs, conforming reduced FD-FEM. (j) 3 LMs, non-conforming reduced FD-FEM. (k) 3 LMs, FD-HiMod with $M = 10$. (l) 3 LMs, FD-HiMod with $M = 20$.

Figure 9: Benchmark case (perfect sink boundary conditions): distribution of the signed pointwise error associated with the conforming (first column) and non-conforming (second column) reduced FD-FEM, and the FD-HiMod (third and fourth columns) approximation, with 1 (first row), 2 (second row), and 3 (third row) LMs.

models, we evaluate the relative error in the $L^2(\Omega_{\mathbf{x},\epsilon})$-norm. Table 1 summarizes this error for the two reduced FD-FEM approximations (conforming and non-conforming) across different mesh sizes h and numbers of LMs, as well as for the FD-HiMod reduced solution when varying h, M, and number of LMs. In line with expectations, regardless of the chosen strategy, increasing the number of LMs or decreasing h leads to a reduction in the error. For the FD-HiMod approximation, a similar behavior is observed when increasing the number M of modal functions. In this case, the interplay between the discretization along Ω_{1D} and the modal discretization becomes evident: the error may stagnate despite refining h if the number of modes is not sufficiently large, and likewise may not decrease by increasing M if the mesh size is not sufficiently small.
The error of the conforming reduced FD-FEM approach represents the asymptotic case, with values that roughly halve as the number of LMs increases, reaching about 12% with 3 LMs. Although this error may appear significant, it should be noted that concentration values remain very low (of the order of 10^{-3}–10^{-2}) across most of the domain under perfect sink conditions. For this boundary data setup, the FD-HiMod approach outperforms the non-conforming reduced FD-FEM for all LMs, even

Table 1: Benchmark case (perfect sink boundary conditions): $L^2(\Omega_{\mathbf{x},\epsilon})$-norm of the relative error associated with the reduced FD-FEM and the FD-HiMod approaches, for different mesh size, number of modes and of LMs.

	conforming reduced **FD-FEM**			non-conforming reduced **FD-FEM**				
N_{LM}	$\mathcal{T}_h^c$			$h = 0.032$	$h = 0.043$	$h = 0.056$	$h = 0.073$	
1	0.30483			0.53517	0.60180	0.71831	0.95308	
2	0.20704			0.37211	0.43236	0.53296	0.77099	
3	0.12017			0.27189	0.29363	0.40450	0.51158	
	FD-HiMod, $h = 0.05$							
N_{LM}	$M = 10$	$M = 15$	$M = 20$	$M = 25$	$M = 30$	$M = 35$	$M = 40$	$M = 45$
1	0.49254	0.42981	0.41443	0.39787	0.38112	0.37525	0.37165	0.36732
2	0.35144	0.30281	0.28906	0.27706	0.26424	0.25963	0.25667	0.25351
3	0.23302	0.18341	0.18110	0.17240	0.16258	0.16161	0.16075	0.15904
	FD-HiMod, $h = 0.025$							
N_{LM}	$M = 10$	$M = 15$	$M = 20$	$M = 25$	$M = 30$	$M = 35$	$M = 40$	$M = 45$
1	0.47721	0.40862	0.39253	0.37579	0.35777	0.35108	0.34738	0.34297
2	0.33838	0.28495	0.27061	0.25883	0.24501	0.24015	0.23723	0.23412
3	0.21308	0.17012	0.16542	0.15499	0.14366	0.14174	0.14044	0.13826
	FD-HiMod, $h = 0.01$							
N_{LM}	$M = 10$	$M = 15$	$M = 20$	$M = 25$	$M = 30$	$M = 35$	$M = 40$	$M = 45$
1	0.47283	0.40236	0.38605	0.36924	0.35052	0.34326	0.33949	0.33503
2	0.33476	0.28013	0.26567	0.25395	0.23963	0.23443	0.23147	0.22835
3	0.20797	0.16713	0.16171	0.15081	0.13901	0.13669	0.13522	0.13288
	FD-HiMod, $h = 0.005$							
N_{LM}	$M = 10$	$M = 15$	$M = 20$	$M = 25$	$M = 30$	$M = 35$	$M = 40$	$M = 45$
1	0.47221	0.40147	0.38512	0.36830	0.34945	0.34209	0.33831	0.33383
2	0.33425	0.27945	0.26498	0.25326	0.23886	0.23359	0.23063	0.22750
3	0.20726	0.16674	0.16122	0.15026	0.13839	0.13601	0.13452	0.13215

in its least accurate configuration ($h = 0.05$, $M = 10$). In the most accurate setting ($h = 0.005$, $M = 45$), a comparison with the conforming reduced FD-FEM asymptotic case shows that the error introduced by the HiMod reduction alone is about 3%, 2%, and 1.2% for 1, 2, and 3 LMs, respectively. Finally, note that results for 2 LMs with $h = 0.02$ are not reported, since this mesh size is not conforming with the partition corresponding to $N_{LM} = 2$.

Figure 10 shows line plots of the relative error, derived from the values reported in Table 1, for the non-conforming reduced FD-FEM with respect to h and for the FD-HiMod approach with respect to M, as the number, N_{LM}, of LMs varies. The plots confirm the observations drawn from the tabulated data. The error decreases very slowly for both reduced FD-FEM and FD-HiMod approaches, likely due to the complexity of the FD setup combined with a discontinuity at the boundary Γ_w (even though it is weakly imposed). In particular, for FD-HiMod the error stagnates starting from approximately 30 modes. This trend differs from the zero flux case, as will be discussed in Section 4.1.2.

For completeness, in Figure 11 we compare the performance of reduced FD-FEM and FD-HiMod methods in terms of the number of DOFs, computed as in (27), for different choices of N_{LM}. The conforming reduced FD-FEM approximation provides the best overall accuracy, with its error represented as a horizontal dashed line serving as a baseline for the other approaches, although this configuration involves approximately $23,000$ DOFs due to the targeted mesh refinement adopted in

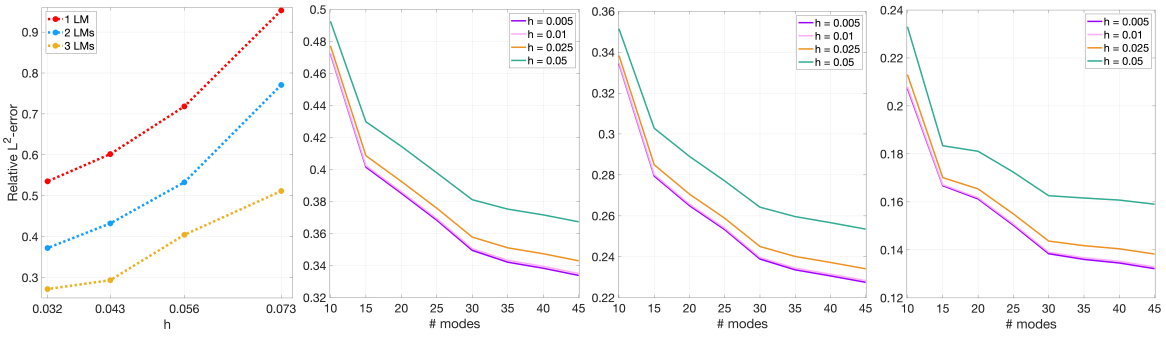

(a) non-conforming reduced FD-FEM. (b) FD-HiMod, for 1 LM. (c) FD-HiMod, for 2 LMs. (d) FD-HiMod, for 3 LMs.

Figure 10: Benchmark case (perfect sink boundary conditions): $L^2(\Omega_{\mathbf{x},\epsilon})$-norm of the relative error for the non-conforming reduced FD-FEM scheme with respect to h and for the FD-HiMod approach with respect to M and for different values of h, when varying the number of LMs.

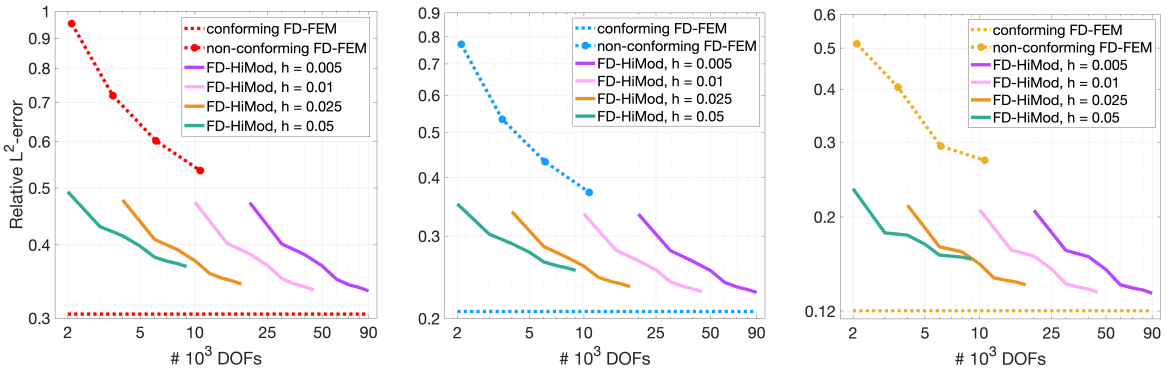

(a) $N_{LM} = 1$. (b) $N_{LM} = 2$. (c) $N_{LM} = 3$.

Figure 11: Benchmark case (perfect sink boundary condition): $L^2(\Omega_{\mathbf{x},\epsilon})$-norm of the relative error for the conforming and non-conforming reduced FD-FEM with respect to #DOFs and for the FD-HiMod approach with respect to #DOFs and for different values of h, when varying the number of LMs.

the conforming setup. In the FD-HiMod case, for a fixed h and N_{LM}, the error decreases with the increase in DOFs (i.e., as the number M of modes grows), while increasing the number of LMs reduces the error, essentially at fixed DOFs. Moreover, for a comparable number of DOFs, FD-HiMod consistently outperforms the non-conforming reduced FD-FEM. In particular, apart from the coarsest choice $h = 0.05$, which is clearly unsuitable for accurate results, the behavior of the error curves is similar for different values of h, with a horizontal shift due to the increase in DOFs. The FD-HiMod approach therefore offers greater flexibility, leading to a more favorable error-to-DOFs trade-off. In particular, it allows one to keep a finer mesh (i.e., a smaller h) than in the non-conforming reduced FD-FEM case, especially near the stent where accuracy is crucial, while containing the computational cost by selecting a moderate number M of modes.

4.1.2 Zero Flux Boundary Conditions

In this section, the artery wall is modeled as a membrane in equilibrium with zero flux. This corresponds to imposing homogeneous Neumann boundary conditions on $\widehat{\Gamma}_{w,\epsilon}$ for the advection-diffusion problem (1). Consequently, the boundary portion Γ_D^{AD} involved in (4) reduces to Γ_S, whereas the HiMod modal basis functions in (14) are selected to satisfy homogeneous Neumann conditions on

both Γ_{axi} and Γ_w, i.e.,

$$\phi_k(r) = \cos(\pi(k-1)r) \quad k = 1, \dots, M.$$

Analogously to the perfect sink setting, we investigate the performance of the reduced FD-FEM and FD-HiMod approaches by varying the number of LMs (where, as in the previous test case, we adopt the configuration in Figure 4c with $N_{LM} = 3$) and the mesh size for the reduced FD-FEM scheme, as well as the number of modes for the FD-HiMod formulation.

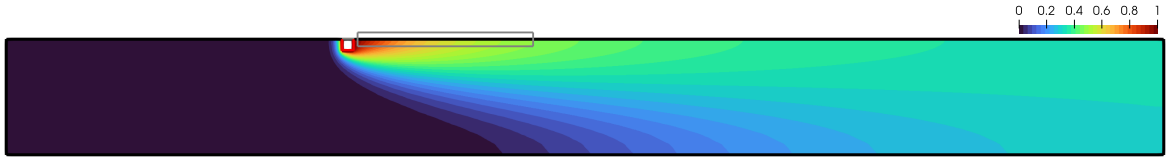

Figure 12: Benchmark case (zero flux boundary condition): reference solution. The gray box highlights the portion of Γ_w selected for the analysis in Figure 13.

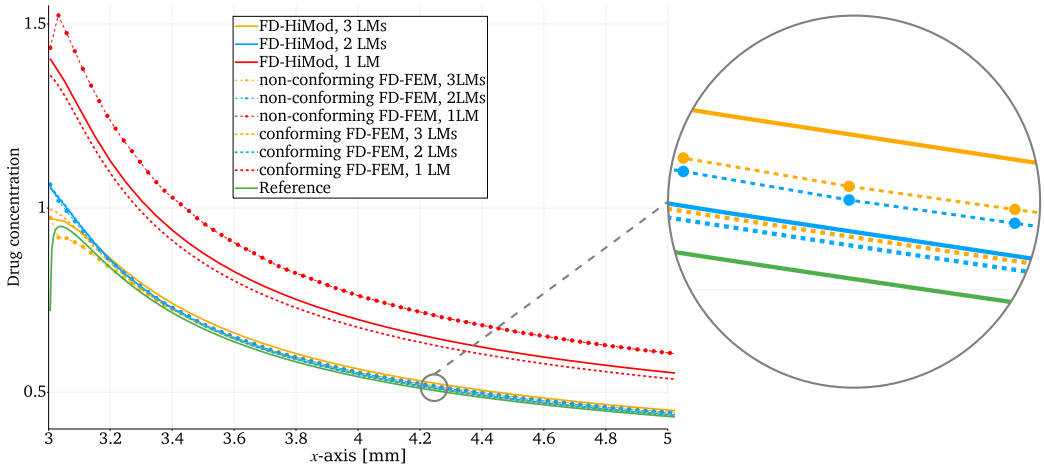

Figure 13: Benchmark case (zero flux boundary condition): comparison of drug distribution along the portion of boundary highlighted in Figure 12 among the reference solution (solid green line), the conforming (dashed lines) and the non-conforming (dotted lines) reduced FD-FEM, and the FD-HiMod (solid lines) approximation for a different number of LMs.

The performance analysis is carried out with respect to the reference solution, c_R, in Figure 12. The different drug concentration distribution resulting from the zero flux boundary condition is evident when compared with the perfect sink setting in Figure 7. The aim here is to model the equilibrium between lumen and arterial wall, where the drug may be absorbed by the wall under specific conditions.
In Figure 13, we compare the reference solution with the conforming/non-conforming reduced FD-FEM and the FD-HiMod approaches, using the same discretizations as in Figure 8. We first observe that solution c_R shows a lower concentration than expected at $x = 3$. This discrepancy is a well-known limitation of standard FE methods, which often struggle to approximate advection-dominated problems, particularly in domains with sharp corners, such as the square stent, and that exhibit boundary discontinuity, such as the imposition of $c = c_0$ on Γ_S [13]. As in the perfect sink configuration, the conforming reduced FD-FEM model remains the most accurate, although it requires the largest number of DOFs (about $23,000$). Unlike in Figure 8, the number of LMs affects accuracy differently.

Specifically, using a single LM leads to a significant overestimation of the drug concentration with respect to the reference values of c_R. In contrast, two and three LMs provide more reliable results, although two LMs yield slightly higher accuracy than three, particularly in the FD-HiMod case. Balancing accuracy and computational cost, the FD-HiMod approximation with two LMs emerges as the best option: it closely follows the reference curve c_R and deviates only slightly from the conforming reduced FD-FEM models with 2 and 3 LMs, while being significantly more efficient than both, requiring only about $6,000$ DOFs instead of $23,000$.

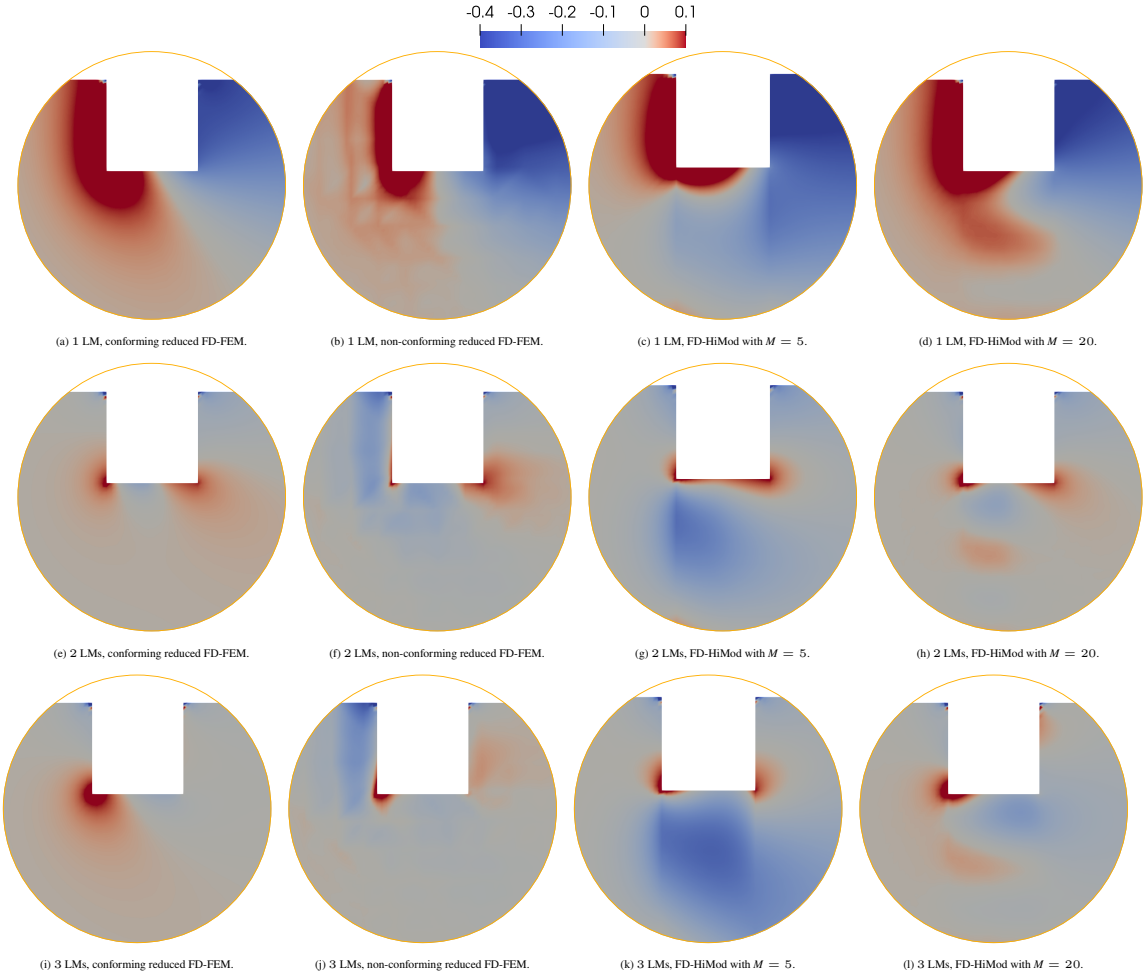

(a) 1 LM, conforming reduced FD-FEM. (b) 1 LM, non-conforming reduced FD-FEM. (c) 1 LM, FD-HiMod with $M = 5$. (d) 1 LM, FD-HiMod with $M = 20$.

(e) 2 LMs, conforming reduced FD-FEM. (f) 2 LMs, non-conforming reduced FD-FEM. (g) 2 LMs, FD-HiMod with $M = 5$. (h) 2 LMs, FD-HiMod with $M = 20$.

(i) 3 LMs, conforming reduced FD-FEM. (j) 3 LMs, non-conforming reduced FD-FEM. (k) 3 LMs, FD-HiMod with $M = 5$. (l) 3 LMs, FD-HiMod with $M = 20$.

Figure 14: Benchmark case (zero flux boundary condition): distribution of the signed pointwise error associated with the conforming (first column), non-conforming (second column) reduced FD-FEM, and the FD-HiMod (third and fourth columns) approximation, with 1 (first row), 2 (second row), and 3 (third row) LMs.

Moving to a qualitative error analysis, Figure 14 shows the distribution of the pointwise signed error between the reference solution c_R and the approximations obtained with the conforming/non-conforming reduced FD-FEM and FD-HiMod approaches. Assigning this new boundary condition improves the accuracy of the approximations compared to the perfect sink configuration, as the overestimation and underestimation with respect to the reference solution is now concentrated at the stent corners rather than spread along its boundary for $N_{LM} = 2, 3$ (compare with Figure 9). This error distribution shows that employing a 3 LM partition (with the three stent sides decoupled) does

not necessarily enhance accuracy compared to the 2 LM configuration. The conforming FD-FEM approximation remains the most accurate also under the zero flux boundary condition, with a further improvement observed when moving from 2 to 3 LMs. Conversely, for a sufficiently large number of modes, the non-conforming reduced FD-FEM and FD-HiMod approximations become comparable, with little to no improvement from increasing the number of LMs from 2 to 3 (in agreement with Figure 13). Interestingly, using only a few modes results in a significant overestimation of the concentration beneath the stent (towards $r = 0$), which is corrected when more modes are employed (compare Figures 14g, 14k with Figures 14h, 14l).

Table 2: Benchmark case (zero flux boundary conditions): $L^2(\Omega_{\mathbf{x},\epsilon})$-norm of the relative error associated with the reduced FD-FEM and the FD-HiMod approaches, for different mesh size, number of modes and of LMs (the 3^* case is omitted for $h = 0.05$, as the associated partition coincides with the 2 LM configuration).

	conforming reduced **FD-FEM**			non-conforming reduced **FD-FEM**				
N_{LM}	$\mathcal{T}_h^c$			$h = 0.032$	$h = 0.043$	$h = 0.056$	$h = 0.073$	$h = 0.099$
1	0.2315			0.37035	0.39275	0.43867	0.48167	0.43688
2	0.0111			0.03228	0.03354	0.04290	0.04973	0.06572
3	0.0128			0.02896	0.04038	0.04096	0.07476	0.07561
3^*	0.0087			0.01765	0.02240	0.03124	0.04918	0.07699
FD-HiMod, $h = 0.05$								
N_{LM}	$M = 5$	$M = 10$	$M = 15$	$M = 20$	$M = 25$	$M = 30$	$M = 35$	$M = 40$	$M = 45$
1	0.39308	0.33106	0.29232	0.28329	0.27337	0.26942	0.26504	0.26284	0.26044
2	0.07924	0.04601	0.02647	0.02241	0.01872	0.01723	0.01586	0.01517	0.01456
3	0.18028	0.12673	0.06805	0.05754	0.04610	0.04184	0.03732	0.03510	0.03278
FD-HiMod, $h = 0.025$								
N_{LM}	$M = 5$	$M = 10$	$M = 15$	$M = 20$	$M = 25$	$M = 30$	$M = 35$	$M = 40$	$M = 45$
1	0.38935	0.32489	0.28529	0.27553	0.26518	0.26093	0.25632	0.25396	0.25143
2	0.07761	0.04467	0.02480	0.02122	0.01750	0.01628	0.01489	0.01433	0.01370
3	0.16471	0.12084	0.06290	0.05254	0.04101	0.03675	0.03213	0.02989	0.02751
3^*	0.10303	0.06716	0.02914	0.02194	0.01560	0.01332	0.01146	0.01080	0.01020
FD-HiMod, $h = 0.01$								
N_{LM}	$M = 5$	$M = 10$	$M = 15$	$M = 20$	$M = 25$	$M = 30$	$M = 35$	$M = 40$	$M = 45$
1	0.38835	0.32319	0.28330	0.27328	0.26276	0.25835	0.25363	0.25117	0.24856
2	0.07723	0.04445	0.02461	0.02119	0.01752	0.01638	0.01504	0.01451	0.01390
3	0.16095	0.11935	0.06160	0.05129	0.03972	0.03546	0.03082	0.02857	0.02617
3^*	0.09133	0.05544	0.02435	0.01911	0.01452	0.01312	0.01103	0.01019	0.00943
FD-HiMod, $h = 0.005$								
N_{LM}	$M = 5$	$M = 10$	$M = 15$	$M = 20$	$M = 25$	$M = 30$	$M = 35$	$M = 40$	$M = 45$
1	0.38821	0.32294	0.28302	0.27295	0.26240	0.25797	0.25324	0.25076	0.24813
2	0.07718	0.04443	0.02459	0.02120	0.01754	0.01641	0.01508	0.01456	0.01395
3	0.16043	0.11914	0.06142	0.05112	0.03954	0.03530	0.03064	0.02839	0.02598
3^*	0.09104	0.05524	0.02424	0.01904	0.01447	0.01308	0.01099	0.01015	0.00940

A quantitative error analysis is reported in Table 2, consistently with the results in Table 1. As a general remark, the relative error values in Table 2 are significantly lower than those in Table 1, in some cases gaining up to one order of magnitude in percentage points. This confirms that, from a modeling perspective, imposing a zero flux condition yields a considerably more accurate approximation of the

drug concentration. In particular, for the conforming and non-conforming reduced FD-FEM models, the error behaves as expected with respect to the mesh size h, reaching errors of about 2% in the non-conforming case and 1% in the conforming case. Increasing the number of LMs from 2 to 3 does not provide the desired improvement, except for the non-conforming case with $h = 0.032$ and $h = 0.056$.
The FD-HiMod approximation confirms its intrinsic modeling flexibility: for sufficiently small h and large M, it achieves a relative error close to 1%, comparable to the conforming reduced FD-FEM case, which remains the asymptotic benchmark also under this boundary condition. Notably, five modes are already sufficient to achieve high accuracy, unlike the perfect sink case where at least ten modes were required to reach a 20% error. As expected, the error decreases both when refining h and when increasing M. No improvement is obtained, however, when moving from 2 to 3 LMs. This may be due to the partition in Figure 4c, which appears unfavorable since the error tends to accumulate at the corners. For this reason, we also tested the alternative partition in Figure 4d, which we denote in the table as the case $N_{LM} = 3^*$. This choice indeed delivers the expected improvement, provided that the HiMod discretization is sufficiently fine (e.g., with $h = 0.025$ and $M \geq 25$, or with $h = 0.01$ or $h = 0.005$ and $M \geq 15$). Likewise, the conforming and non-conforming reduced FD-FEM approaches improve in accuracy with the 3^* setup, provided that the mesh size h is sufficiently small in the non-conforming case (for istance, $h = 0.099$ is too coarse to observe any improvement).

Similarly to the perfect sink case, we analyze the error trend of the reduced FD-FEM and FD-HiMod models based on the values in Table 2. We first examine the effect of mesh refinement in the non-conforming reduced FD-FEM approach and of increasing the number of modes in the FD-HiMod formulation, while varying the number of LMs, as done in Figure 15. The trend across Figures 15a - 15d confirms that using 3 LMs generally provides no benefit, unlike the 3^* LMs case, which can improve accuracy (see Figures 15a and 15d). Note that in Figure 15, a logarithmic scale is used on the vertical axis to improve visual rendering, as the error quickly stagnates for FD-HiMod beyond 30 modes, particularly in the cases with 2 and 3 LMs. Furthermore, compared to the perfect sink case, a much lower sensitivity to the mesh size h is observed in Figures 15b–15d, where the error curves nearly overlap.

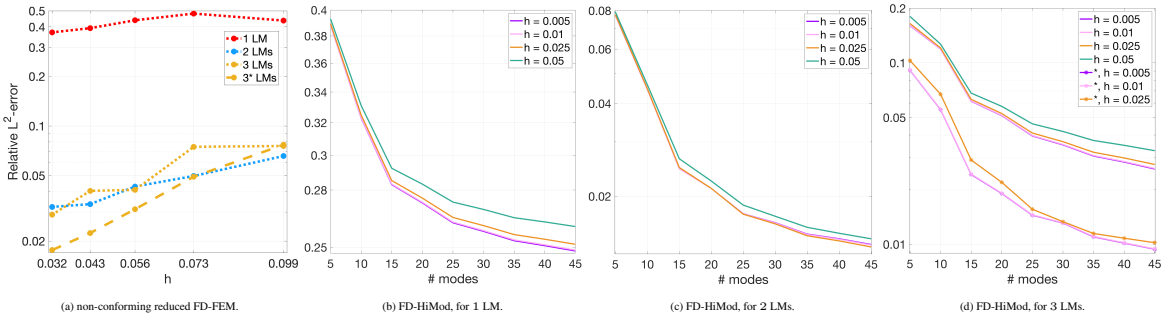

(a) non-conforming reduced FD-FEM. (b) FD-HiMod, for 1 LM. (c) FD-HiMod, for 2 LMs. (d) FD-HiMod, for 3 LMs.

Figure 15: Benchmark case (zero flux boundary condition): $L^2(\Omega_{\mathbf{x},\epsilon})$-norm of the relative error for the non-conforming reduced FD-FEM with respect to h and for the FD-HiMod approach with respect to M and for different values of h, when varying the number of LMs. In the legend, symbol $*$ is associated with the 3 LM partition case in Figure 4d.

The error trend with respect to the number of DOFs is shown in Figure 16, where we perform the same analysis as in Figure 11. Consistently with the perfect sink case, the accuracy improves as the mesh size h decreases for the non-conforming reduced FD-FEM approach, and as the number M of modes increases in the FD-HiMod formulation, while the conforming FD-FEM remains the reference case also under zero flux boundary conditions. However, unlike the perfect sink configuration, the FD-HiMod outperforms the non-conforming reduced FD-FEM method only when the HiMod approximation is sufficiently refined. In agreement with Table 2 and Figure 15, we also observe that the

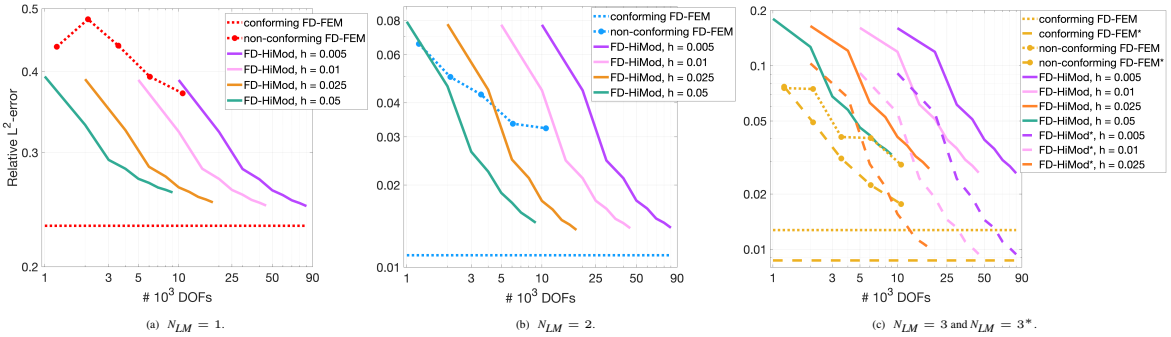

(a) $N_{LM} = 1$. (b) $N_{LM} = 2$. (c) $N_{LM} = 3$ and $N_{LM} = 3^*$.

Figure 16: Benchmark case (zero flux boundary condition): $L^2(\Omega_{\mathbf{x},\epsilon})$-norm of the relative error for the conforming and non-conforming reduced FD-FEM with respect to #DOFs and for the FD-HiMod approach with respect to #DOFs and for different values of h, when varying the number of LMs.

use of 3 LMs does not necessarily improve the accuracy of the non-conforming reduced FD-FEM and FD-Himod approximations, unless the 3^* LM partition in Figure 4d, coupling the three stent sides, is adopted. As shown in Figure 16c, in this last configuration FD-HiMod achieves an accuracy very close to that of the conforming reduced FD-FEM: for suitable combinations of h and M, the errors are only 1-3% larger than the conforming asymptotic values while requiring significantly fewer DOFs ($6,000$-$12,000$ versus $23,000$). For larger DOF counts ($15,000$-$23,000$), other choices of h and M even allow FD-HiMod to attain errors lower than those of the conforming reduced FD-FEM evaluated on the 3 LM partition in Figure 4c, which decouples the three stent sides. Moreover, for $h = 0.025$ selecting appropriate modes M yields errors close to the asymptotic level (about 1%) already for $15,000$-$18,000$ DOFs, even compared to the conforming reduced FD-FEM that couples the stent sides.

4.2 The production case

In this setting, we consider a more realistic scenario where the advective field $\mathbf{u}$ models blood flow in a coronary artery. Specifically, we solve system (2) with a parabolic inflow profile $\mathbf{f}$ and the advection-diffusion model (1) with a zero flux boundary condition on Γ_w, thus simulating drug release under physiological conditions with a Reynolds number about equal to 100 and a Péclet number greater than one. The analysis focuses on the drug concentration along Γ_w, since the drug is rapidly advected by the flow and mainly diffuses near the artery wall, where it is absorbed. Indeed, the total amount of absorbed drug on Γ_w is directly related to treatment efficacy in preventing restenosis, making accurate simulations crucial for optimizing stent design and drug-release strategies.
To investigate how strut configurations affect the model performance under these conditions, we introduce three rings placed at varying mutual distances. This choice allows us to evaluate the sensitivity of the approximations to obstacle spacing, a relevant factor in realistic stent geometries where struts may be positioned either close together or further apart, with different physiological implications.
Concerning the number of LMs, we set $N_{LM} = 2$, motivated by the benchmark results: two LMs yield satisfactory accuracy, often comparable to three, while significantly outperforming the one LM case.

Figure 17 shows the reference solution c_R for three equidistant rings. The distances between the first and second and between the second and third ring are denoted by d_1 and d_2, respectively, with the first ring closest to the inflow boundary Γ_{in} and the third ring closest to the outflow boundary Γ_{out}. To study the sensitivity of the solution with respect to d_1 and d_2, we vary their values by taking $d_1, d_2 \in \{0.3, 1, 2\}$. In practice, the position of the second ring is fixed at $x = 5$, while the first

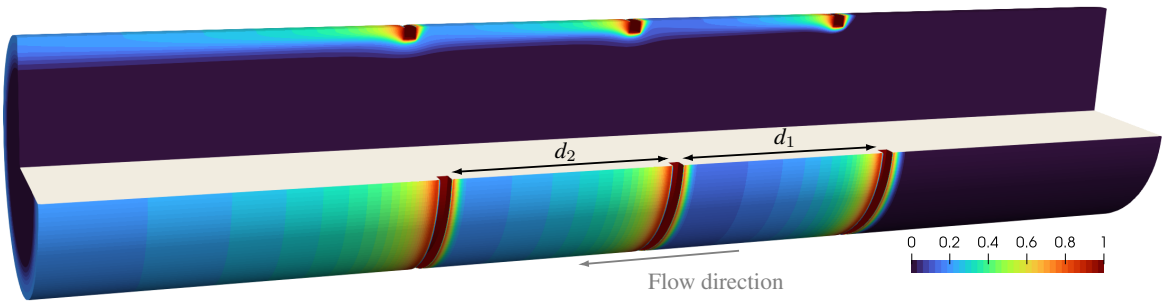

Figure 17: The production case: reference solution c_R for three equidistant stent rings, with inter-ring spacings $d_1 = d_2 = 2$.

and third rings are shifted accordingly. We recall that the lumen segment is assumed to be 10 mm long, placing the second ring at the midpoint of the vessel. The maximum distance $d = 2$ is chosen because, at this spacing, the rings can be considered effectively independent: in this case, the drug concentration downstream of two rings matches that obtained with a single one-ring stent placed at the same distance from the outflow. Conversely, the minimum distance $d = 0.3$ is selected to remain consistent with the mesh resolution and to ensure a meaningful solution, avoiding degenerate cases where $c_R = 1$ on Γ_w between rings.

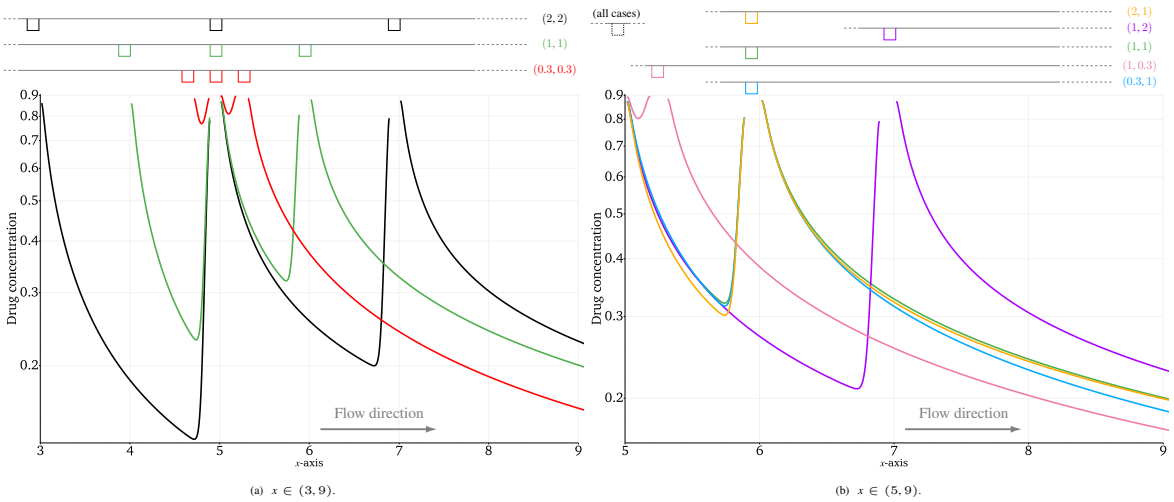

(a) $x \in (3, 9)$. (b) $x \in (5, 9)$.

Figure 18: The production case: drug distribution of the reference solution along the wall Γ_w for different choices of (d_1, d_2), with symmetric (left) and asymmetric (right) ring arrangements. Above each plot, a color-coded sketch illustrates the corresponding ring positions (schematic, not to scale).

The main focus of Figure 18 is to show the non-zero drug concentration along the artery wall Γ_w. Since upstream values are always zero, all plots start at $x > 3$, just after the first ring (for $d_1 = 2$). Figure 18a shows reference solutions c_R for equidistant rings, with $(d_1, d_2) = (2, 2), (1, 1), (0.3, 0.3)$. As d_1 and d_2 decrease, concentration increases between the rings but decreases at the outflow. Figure 18b compares four asymmetric configurations, namely $(d_1, d_2) = (1, 2), (2, 1), (0.3, 1), (1, 0.3)$, with the equidistant configuration $(d_1, d_2) = (1, 1)$ in Figure 18a. We restrict our attention to $x > 5$, since the profile between the first and second rings remains almost unchanged when varying d_2 at fixed d_1. In fact, upstream concentrations are insensitive to downstream spacing due to the highly advective regime. When $d_2 = 1$ is fixed and d_1 varies, only minor changes appear: a small reduction between

the first and second rings for $d_1 = 2$, and a decrease near the outflow for $d_1 = 0.3$. In contrast, fixing $d_1 = 1$ and varying d_2 produces marked differences along the whole wall, with lower concentrations at the outflow as d_2 decreases.

We now investigate the performance of the non-conforming reduced FD-FEM and FD-HiMod approaches by computing the $L^2(\Omega_{\mathbf{x},\epsilon})$-norm of the relative error with respect to c_R. We vary the mesh size $h \in \{0.032, 0.043, 0.056, 0.073\}$ for FD-FEM, while both $h \in \{0.05, 0.025, 0.01, 0.005\}$ and $M \in \{10, 15, 20, 25, 30\}$ for FD-HiMod. The complete set of error values is reported in Table 3. Errors range between 10% and 15%, less satisfactory than in the benchmark case, likely due to the more complex advection field and geometric configuration. In general, the error decreases as expected: for FD-FEM it reduces with mesh refinement, while for FD-HiMod it decreases either with smaller h (provided M is sufficiently large) or with larger M (for sufficiently small h). Although no clear global trend emerges with respect to the ring distances, equidistant configurations appear slightly more accurate, particularly for the choice $(d_1, d_2) = (1, 1)$. Conversely, strongly asymmetric placements, such as $(d_1, d_2) = (0.3, 2)$, tend to yield larger errors, especially when the closest ring is upstream.

Table 3: The production case: $L^2(\Omega_{\mathbf{x},\epsilon})$-norm of the relative error associated with the non-conforming reduced FD-FEM and FD-HiMod approaches, for different mesh size, number of modes and ring distances (d_1, d_2).

(d_1, d_2)	$(2, 2)$	$(1, 2)$	$(0.3, 2)$	$(2, 1)$	$(1, 1)$	$(0.3, 1)$	$(2, 0.3)$	$(1, 0.3)$	$(0.3, 0.3)$
non-conforming FD-FEM, $h = 0.032$	0.10690	0.10159	0.11010	0.10155	0.09641	0.10443	0.10570	0.10002	0.10767
non-conforming FD-FEM, $h = 0.043$	0.13060	0.12891	0.12237	0.12372	0.12352	0.11636	0.12542	0.12519	0.11869
non-conforming FD-FEM, $h = 0.056$	0.21873	0.18213	0.18469	0.20415	0.19821	0.17007	0.19455	0.18172	0.16280
non-conforming FD-FEM, $h = 0.073$	0.22211	0.19329	0.19591	0.24044	0.20983	0.21572	0.21350	0.18971	0.18462
FD-HiMod, $h = 0.05$, $M = 10$	0.17963	0.17328	0.18444	0.16980	0.16470	0.17539	0.16796	0.16416	0.17561
FD-HiMod, $h = 0.05$, $M = 15$	0.16222	0.15688	0.15773	0.15795	0.15136	0.14973	0.15191	0.14810	0.14840
FD-HiMod, $h = 0.05$, $M = 20$	0.13924	0.13856	0.14270	0.13946	0.13671	0.13765	0.13689	0.13648	0.13955
FD-HiMod, $h = 0.05$, $M = 25$	0.13255	0.13334	0.13835	0.13445	0.13226	0.13313	0.13134	0.13115	0.13499
FD-HiMod, $h = 0.05$, $M = 30$	0.13297	0.13401	0.13866	0.13512	0.13297	0.13314	0.13141	0.13149	0.13488
FD-HiMod, $h = 0.025$, $M = 10$	0.16787	0.16199	0.17383	0.16015	0.15572	0.16718	0.15986	0.15610	0.16858
FD-HiMod, $h = 0.025$, $M = 15$	0.15011	0.14490	0.14664	0.14507	0.13902	0.13865	0.13884	0.13428	0.13485
FD-HiMod, $h = 0.025$, $M = 20$	0.12444	0.12406	0.12955	0.12447	0.12171	0.12470	0.12155	0.11968	0.12380
FD-HiMod, $h = 0.025$, $M = 25$	0.11782	0.11960	0.12499	0.11941	0.11732	0.11988	0.11657	0.11501	0.11934
FD-HiMod, $h = 0.025$, $M = 30$	0.11750	0.11930	0.12479	0.11926	0.11703	0.11953	0.11612	0.11447	0.11880
FD-HiMod, $h = 0.01$, $M = 10$	0.15357	0.14933	0.16197	0.14714	0.14371	0.15554	0.15115	0.14736	0.16081
FD-HiMod, $h = 0.01$, $M = 15$	0.13853	0.13263	0.13438	0.13237	0.12560	0.12564	0.12850	0.12295	0.12287
FD-HiMod, $h = 0.01$, $M = 20$	0.11421	0.11225	0.11742	0.11267	0.10882	0.11259	0.11137	0.10902	0.11212
FD-HiMod, $h = 0.01$, $M = 25$	0.10890	0.10806	0.11265	0.10888	0.10486	0.10819	0.10687	0.10492	0.10767
FD-HiMod, $h = 0.01$, $M = 30$	0.10826	0.10747	0.11201	0.10843	0.10432	0.10768	0.10627	0.10435	0.10711
FD-HiMod, $h = 0.005$, $M = 10$	0.15077	0.14648	0.15915	0.14483	0.14125	0.15336	0.14981	0.14616	0.16001
FD-HiMod, $h = 0.005$, $M = 15$	0.13683	0.13090	0.13215	0.12982	0.12330	0.12378	0.12768	0.12224	0.12248
FD-HiMod, $h = 0.005$, $M = 20$	0.11303	0.11110	0.11577	0.11038	0.10681	0.11115	0.11102	0.10863	0.11186
FD-HiMod, $h = 0.005$, $M = 25$	0.10837	0.10735	0.11125	0.10679	0.10301	0.10726	0.10708	0.10513	0.10773
FD-HiMod, $h = 0.005$, $M = 30$	0.10763	0.10670	0.11058	0.10624	0.10233	0.10671	0.10646	0.10451	0.10709

To offer a more concise overview of the sensitivity of the solution to the parameters (d_1, d_2), we provide in Figure 19 the boxplots of the average concentration $\bar{c}$ over the entire domain (see Figure 19a) and $\bar{c}_w$ along the downstream section of the wall Γ_w (see Figure 19b). We analyze the nine combinations of ring distances (d_1, d_2) through the variability introduced by the non-conforming reduced FD-FEM (compact blue boxplots, with medians marked by blue circles) and FD-HiMod (standard boxplots) methods, when varying mesh size h and number M of modes. Trends are assessed by comparing changes in the median values across different spacing configurations. For each case, the downstream section of Γ_w considered corresponds to the stent-free region with non-zero drug concentration (e.g., measurements start at $x = 3$ for $(d_1, d_2) = (2, 2)$, and at $x = 4.7$ for $(d_1, d_2) = (0.3, 0.3)$), ensuring that upstream zero-concentration regions do not bias comparisons.
Figure 19a shows that the non-conforming reduced FD-FEM method generally predicts higher average concentrations than FD-HiMod across all (d_1, d_2) configurations, and exhibits greater variability likely because only four mesh sizes h are tested, whereas FD-HiMod explores 20 combinations of h and M values. The median value of $\bar{c}$ appears more sensitive to d_1 than to d_2. Grouping the boxplots from left to right (with $d_2 = 2$, 1, 0.3, respectively), we observe a consistent decrease in $\bar{c}$ as d_1 decreases from 2 to 0.3, while changes in d_2 have a smaller effect. The configuration $(0.3, 0.3)$ produces the

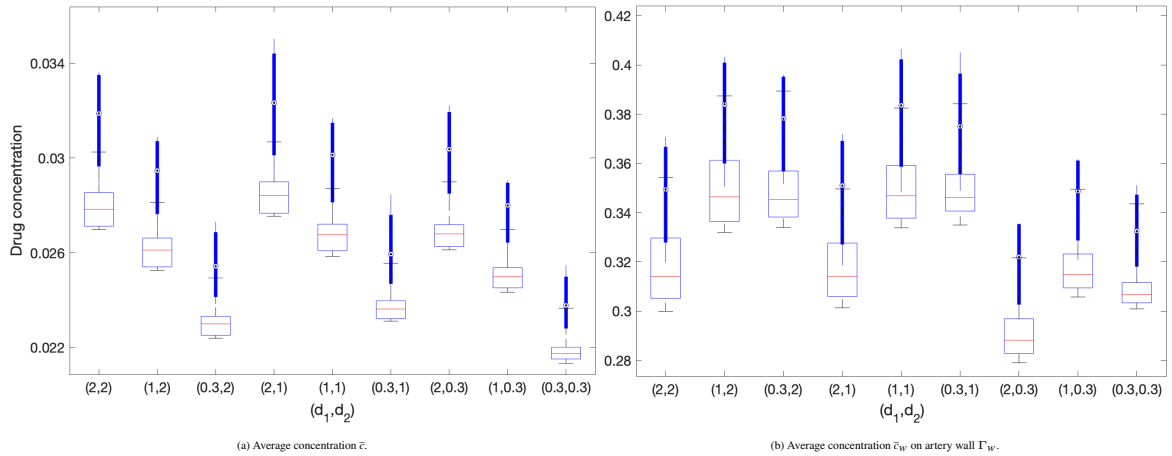

(a) Average concentration $\bar{c}$.

(b) Average concentration $\bar{c}_W$ on artery wall Γ_W.

Figure 19: The production case: average concentration over the entire domain (on the left) and along the artery wall (on the right) associated with the non-conforming reduced FD-FEM (compact boxplots) and the FD-HiMod (standard bloxplots) approaches, for different (d_1, d_2) configurations.

lowest concentration overall, whereas moderate spacing between rings ($\sim$ 1 mm) tends to maximize $\bar{c}$. Since most of the drug accumulates near the artery wall and the domain concentration is otherwise close to zero, with $\bar{c}$ of order 10^{-2}, this average value can be interpreted as the fraction of drug washed out into the bloodstream and lost after release.

Focusing on the effective drug delivered to the artery wall in Figure 19b, we observe trends similar to those in Figure 19a. Non-conforming reduced FD-FEM generally overestimates $\bar{c}_w$ compared to FD-HiMod, while both approaches show greater variability when the three rings are further apart, i.e., for $d_1 > 0.3$ and $d_2 > 0.3$., reflecting its sensitivity to both the mesh size h and the number M of modes, except when the three rings are very close. When d_2 is fixed, $\bar{c}_w$ is noticeably affected by reducing d_1 from 2 to smaller values (1 or 0.3), though differences between $d_1 = 1$ and $d_1 = 0.3$ are minor. The median $\bar{c}_w$ is higher when the two upstream rings are closer. Conversely, fixing $d_1 = 2$ yields little change between $d_2 = 2$ and $d_2 = 1$, but a marked decrease at $d_2 = 0.3$. The same decreasing trend appears when fixing $d_1 = 1$ or 0.3 and reducing d_2. Overall, drug delivery to the wall is maximized when the upstream rings are close together, while the third ring is kept at a moderate distance ($d_2 = 1$ or 2).

4.3 Discussion

The benchmark and production cases confirm the effectiveness of the FD approach combined with Hi-Mod reduction in handling complex geometries, such as arteries with stent-induced obstacles. Overall, FD-HiMod provides a balanced solution compared to the reduced FD-FEM models: in particular, FD-HiMod outperforms the non-conforming case, while being only slightly less accurate than the conforming version, which however comes at a prohibitive computational cost in terms of DOFs. Thus, FD-HiMod achieves the desired trade-off between accuracy and efficiency.

As expected from the model formulation, FD-HiMod accuracy depends on the number of LMs, the mesh size h, and the number M of modes. We recover the interplay already observed in other contexts: accuracy improves as h decreases (provided M is sufficiently large) and as M increases (provided h is sufficiently small). The optimal choice of N_{LM} is less straightforward, since simply increasing the number of LMs does not necessarily lead to better results.

Based on our observations, the optimal number of LMs depends on the type of boundary condition assigned on the stent. Two cases were considered: a perfect sink (Dirichlet) condition, representing

complete drug absorption by the artery wall, and a zero flux (Neumann) condition, simulating an intermediate equilibrium suitable for hydrophobic drugs with staggered lumen-wall absorption. In general, weak Dirichlet boundary conditions can be employed in a conforming immersed approach to overcome the limitations of classical FEM, which struggles to capture discontinuities in (1). In particular, the reduced interface condition on Γ_S in (10), consisting of a low-degree LM function space, is well-suited for small obstacles, such as stents, and for setups with discontinuities between wall and stent. Thus, adding LMs along the stent boundary improves the approximation of the jump at the stent-artery interface. In contrast, under a zero flux boundary condition, the concentration difference at the stent-wall interface is less abrupt, so increasing the number of LMs does not necessarily enhance accuracy. A comparison between Figure 9 and Figure 14 confirms that for perfect sink conditions, the error concentrates around the stent edges, with overshoots and undershoots, whereas for zero flux conditions it is mainly localized at the stent corners. Hence, to improve the error distribution when increasing the number of LMs, a tailored three LM partitioning strategy that couples the stent edges is required (see Figure 16c).
Examining the global accuracy of the conforming reduced FD-FEM and FD-HiMod approaches, we observe that two LMs are already sufficient to achieve an $L^2(\Omega_{\mathbf{x},\epsilon})$ norm of the relative error of about 1% for the zero flux case (see Table 2 and Figure 16b). By contrast, the error is significantly higher under perfect sink conditions as highlighted by the values in Table 1. However, given that the average concentration $\bar{c}$ is small (on the order of 10^{-2}), a 20% relative error corresponds to an absolute difference of only about 0.002, as confirmed by the qualitative comparison in Figure (8).
The analysis of the more complex scenario with realistic flow conditions, using a three-ring stent configuration, showed that the placement of the stent rings has a significant impact on the potential effectiveness of the therapy. In particular, Figure 18 illustrates how the local drug distribution along Γ_w is influenced by the ring position. If a higher drug concentration near the stent is desired, the rings should be placed closer together. Conversely, if drug release further downstream is preferred, the rings should be spaced farther apart. In the case of anti-proliferative drugs, achieving a higher concentration near the injured artery wall is particularly important, making closely spaced struts more suitable for this purpose. Specifically, regarding the quantities analyzed in Figure 19, the average drug concentration on the artery wall, $\bar{c}_w$, plays the predominant role in this sensitivity analysis with respect to ring placement, whereas the average concentration across the entire domain, $\bar{c}$, remains an important metric for assessing how much drug is washed out and lost into the bloodstream. Thus, if minimizing drug washout is the primary goal, the $(0.3, 0.3)$ configuration is optimal, even though it delivers less drug on average to the artery wall. Conversely, if a more homogeneous and higher delivery along the artery wall is desired, evenly spaced rings, such as $(1, 1)$ and $(1, 2)$, provide the best results.

5 Conclusions

This study evaluates the effectiveness of the FD-HiMod approach in reducing computational costs while preserving solution accuracy when modeling complex geometries with obstacles much smaller than the overall domain, such as stented arteries. While HiMod reduction has already proven effective in various applications, ranging from blood flow modeling and linear acoustics to electromagnetism, it is generally restricted to sufficiently smooth domains. This limitation arises from regularity constraints on the mapping from the physical to the reference domain, which exclude geometries with sharp features, such as an artery lumen containing stents. The main contribution of this work is to combine the FD approach with HiMod, enabling HiMod to handle complex geometries while enhancing a standard FD (e.g., FEM) formulation to reduce its computational effort. In particular, the results of the production case demonstrate that the FD-HiMod approach effectively captures drug transport dynamics in near-realistic scenarios, while keeping computational costs significantly lower than conforming reduced FD-FEM simulations. Moreover, the sensitivity analysis with respect to

strut configuration carried out in Section 4.2 highlights the strong dependence of drug distribution on ring spacing, emphasizing the crucial role of stent design parameters in ensuring effective drug release.

This work should be regarded as a proof-of-concept for the FD-HiMod approach. Several extensions could be pursued to increase its applicability, such as including drug diffusion into the arterial wall (requiring the imposition of Robin-type boundary conditions instead of Dirichlet and Neumann data), moving beyond the lumen-only setting, and addressing unsteady regimes. Further research should also address more realistic artery geometries, stent designs, and patient-specific flow conditions, ultimately enhancing the clinical relevance of the method and exploring its potential extension to full blood flow modeling with the Navier-Stokes equations. Lastly, a natural direction for future work could be to develop a rigorous convergence theory for the considered FD formulations, thereby strengthening their mathematical and modeling foundations.

Funding statement

This work was funded by the German Research Foundation (DFG) – project number 465213526 (subproject "In-stent restenosis in coronary arteries – computational and data-driven investigations towards translational modeling" of SPP 2311).

Acknowledgments

AR was partly supported by the IRTG Modern Inverse Problems which is funded by the DFG – 333849990/GRK2379. FL and PZ acknowledge the support of the grant MUR PRIN 2022 No. 2022WKWZA8 Immersed methods for multiscale and multiphysics problems (IMMEDIATE) funded by the Next Generation EU Program, Mission 4, Comp. 2, CUP D53D23006010006. SP and PZ acknowledge the support by MUR, grant Dipartimento di Eccellenza 2023-2027. FB, SP and PZ are members of the Gruppo Nazionale Calcolo Scientifico-Istituto Nazionale di Alta Matematica (GNCS-INdAM). AR, PZ and SP also acknowledge the IDEA League Research Grant "Model reduction in arteries with drug-eluting stents".

Author contributions

AR: conceptualization; formal analysis; investigation; methodology; project administration; software; validation; visualization; writing – original draft (lead); writing – review & editing.
FB: formal analysis; supervision; writing – original draft; writing – review & editing.
FL: formal analysis; investigation; software; writing – original draft; writing – review & editing.
PZ: conceptualization; methodology; supervision; writing – review & editing.
SP: conceptualization; formal analysis; methodology; supervision; writing – review & editing.

Conflict of interest

The authors declare no potential conflict of interests.

Data availability statement

Scripts and additional data are available from the corresponding author upon reasonable request.

References

[1] Matteo C. Aletti, Simona Perotto, and Alessandro Veneziani. HiMod reduction of advection-diffusion-reaction problems with general boundary conditions. *Journal of Scientific Computing*, 76:89–119, 2018.

[2] Brinda Balakrishnan, John F Dooley, Gregory Kopia, and Elazer R Edelman. Intravascular drug release kinetics dictate arterial drug deposition, retention, and distribution. *Journal of Controlled Release*, 123:100–108, 2007.

[3] Zakaria Belhachmi, Christine Bernardi, and Simone Deparis. Weighted clément operator and application to the finite element discretization of the axisymmetric stokes problem. *Numerische Mathematik*, 105:217–247, 2006.

[4] Daniele Boffi, Nicola Cavallini, and Lucia Gastaldi. The finite element immersed boundary method with distributed lagrange multiplier. *SIAM Journal on Numerical Analysis*, 53:2584–2604, 2015.

[5] Muriel Boulakia, Céline Grandmont, Fabien Lespagnol, and Paolo Zunino. Mathematical and numerical analysis of reduced order interface conditions and augmented finite elements for mixed dimensional problems. *Computers and Mathematics with Applications*, 175:536–569, 2024.

[6] James H Bramble. The lagrange multiplier method for dirichlet's problem. *Mathematics of Computation*, 37:1–11, 1981.

[7] Yves Antonio Brandes Costa Barbosa and Simona Perotto. Hierarchically reduced models for the Stokes problem in patient-specific artery segments. *International Journal of Computational Fluid Dynamics*, 34:160–171, 2020.

[8] Claudio Chiastra, Stefano Morlacchi, Diego Gallo, Umberto Morbiducci, Rubén Cárdenes, Ignacio Larrabide, and Francesco Migliavacca. Computational fluid dynamic simulations of image-based stented coronary bifurcation models. *Journal of The Royal Society Interface*, 10:20130193, 2013.

[9] Giovanni Conni, Stefano Piccardo, Simona Perotto, Giovanni M. Porta, and Matteo Icardi. Hiphome: High order projection-based homogenisation for advection diffusion reaction problems. *Multiscale Modeling & Simulation*, 23:640–667, 2025.

[10] Anne Cornelissen, Roberta Andreea Florescu, Stefanie Reese, Marek Behr, Anna Ranno, Kiran Manjunatha, Nicole Schaaps, Christian Böhm, Elisa Anamaria Liehn, Liguo Zhao, et al. In-vivo assessment of vascular injury for the prediction of in-stent restenosis. *International Journal of Cardiology*, 388:131151, 2023.

[11] Anna Corti, Monika Colombo, Francesco Migliavacca, Jose Felix Rodriguez Matas, Stefano Casarin, and Claudio Chiastra. Multiscale computational modeling of vascular adaptation: a systems biology approach using agent-based models. *Frontiers in Bioengineering and Biotechnology*, 9:744560, 2021.

[12] Elena Cutrì, Paolo Zunino, Stefano Morlacchi, Claudio Chiastra, and Francesco Migliavacca. Drug delivery patterns for different stenting techniques in coronary bifurcations: a comparative computational study. *Biomechanics and modeling in mechanobiology*, 12:657–669, 2013.

[13] Jean Donea and Antonio Huerta. *Finite element methods for flow problems*. John Wiley & Sons, 2003.

[14] Alexandre Ern, Simona Perotto, and Alessandro Veneziani. Hierarchical model reduction for advection-diffusion-reaction problems. In *Numerical Mathematics and Advanced Applications*, pages 703–710. Springer, 2008.

[15] Vasim Farooq, Bill D Gogas, and Patrick W Serruys. Restenosis: delineating the numerous causes of drug-eluting stent restenosis. *Circulation: Cardiovascular Interventions*, 4:195–205, 2011.

[16] G. Garcia-Contreras, J. Córcoles, J. A. Ruiz-Cruz, M. Oldoni, G. G. Gentili, S. Micheletti, and S. Perotto. Advanced modeling of rectangular waveguide devices with smooth profiles by hierarchical model reduction. *IEEE Transactions on Microwave Theory and Techniques*, 71:4692–4702, 2023.

[17] G. G. Gentili, M. Khosronejad, G. Bernasconi, S. Perotto, and S. Micheletti. Efficient modeling of multimode guided acoustic wave propagation in deformed pipelines by hierarchical model reduction. *Applied Numerical Mathematics*, 173:329–344, 2022.

[18] Omar Ghattas and Karen Willcox. Learning physics-based models from data: perspectives from inverse problems and model reduction. *Acta Numerica*, 30:445–554, 2021.

[19] R Glowinski and Yu Kuznetsov. Distributed lagrange multipliers based on fictitious domain method for second order elliptic problems. *Computer Methods in Applied Mechanics and Engineering*, 196:1498–1506, 2007.

[20] Roland Glowinski, T-W Pan, Todd I Hesla, and Daniel D Joseph. A distributed lagrange multiplier/fictitious domain method for particulate flows. *International Journal of Multiphase Flow*, 25:755–794, 1999.

[21] Sofia Guzzetti, Simona Perotto, and Alessandro Veneziani. Hierarchical model reduction for incompressible fluids in pipes. *International Journal for Numerical Methods in Engineering*, 114:469–500, 2018.

[22] Nora Hagmeyer, Matthias Mayr, and Alexander Popp. A fully coupled regularized mortar-type finite element approach for embedding one-dimensional fibers into three-dimensional fluid flow. *International Journal for Numerical Methods in Engineering*, 125:e7435, 2024.

[23] Nora Hagmeyer, Matthias Mayr, Ivo Steinbrecher, and Alexander Popp. One-way coupled fluid-beam interaction: capturing the effect of embedded slender bodies on global fluid flow and vice versa. *Advanced Modeling and Simulation in Engineering Sciences*, 9:9, 2022.

[24] Stefan Haßler, Lutz Pauli, and Marek Behr. The variational multiscale formulation for the fully-implicit log-morphology equation as a tensor-based blood damage model. *International Journal for Numerical Methods in Biomedical Engineering*, 35:e3262, 2019.

[25] Luca Heltai and Paolo Zunino. Reduced lagrange multiplier approach for non-matching coupling of mixed-dimensional domains. *Mathematical Models and Methods in Applied Sciences*, 33:2425–2462, 2023.

[26] Jan S Hesthaven, Gianluigi Rozza, and Benjamin Stamm. *Certified reduced basis methods for parametrized partial differential equations*, volume 590. Springer, 2016.

[27] DR Hose, AJ Narracott, B Griffiths, S Mahmood, J Gunn, D Sweeney, and PV Lawford. A thermal analogy for modelling drug elution from cardiovascular stents. *Computer methods in biomechanics and biomedical engineering*, 7:257–264, 2004.

[28] Chao-Wei Hwang, David Wu, and Elazer R Edelman. Physiological transport forces govern drug distribution for stent-based delivery. *Circulation*, 104:600–605, 2001.

[29] Violeta Karyofylli, Liubov Kamaldinova, Marek Simon, Oleg Mokrov, Uwe Reisgen, and Marek Behr. Axisymmetric two-phase flow simulations on space-time meshes. *PAMM*, 19:e201900409, 2019.

[30] Kumaran Kolandaivelu, Benjamin B Leiden, and Elazer R Edelman. Predicting response to endovascular therapies: dissecting the roles of local lesion complexity, systemic comorbidity, and clinical uncertainty. *Journal of biomechanics*, 47:908–921, 2014.

[31] Miroslav Kuchta, Federica Laurino, Kent-Andre Mardal, and Paolo Zunino. Analysis and approximation of mixed-dimensional pdes on 3d-1d domains coupled with lagrange multipliers. *SIAM Journal on Numerical Analysis*, 59:558–582, 2021.

[32] Fabien Lespagnol, Céline Grandmont, Paolo Zunino, and Miguel A Fernández. A mixed-dimensional formulation for the simulation of slender structures immersed in an incompressible flow. *Computer Methods in Applied Mechanics and Engineering*, 432:117316, 2024.

[33] Massimiliano Lupo Pasini and Simona Perotto. Hierarchical model reduction driven by a proper orthogonal decomposition for parametrized advection-diffusion-reaction problems. *Electronic Transactions on Numerical Analysis*, 55:187–212, 2022.

[34] Massimiliano Lupo Pasini and Simona Perotto. Hierarchical model reduction driven by machine learning for parametric advection-diffusion-reaction problems in the presence of noisy data. *Journal of Scientific Computing*, 94:36, 2023.

[35] Kiran Manjunatha, Anna Ranno, Jianye Shi, Nicole Schaaps, Pakhwan Nilcham, Anne Cornelissen, Felix Vogt, Marek Behr, and Stefanie Reese. A continuum chemo-mechano-biological model for in-stent restenosis with consideration of hemodynamic effects. *GAMM-Mitteilungen*, 48:e202370008, 2024.

[36] Kiran Manjunatha, Nicole Schaaps, Marek Behr, Felix Vogt, and Stefanie Reese. Computational modeling of in-stent restenosis: Pharmacokinetic and pharmacodynamic evaluation. *Computers in Biology and Medicine*, 167:107686, 2023.

[37] Sean McGinty. A decade of modelling drug release from arterial stents. *Mathematical biosciences*, 257:80–90, 2014.

[38] Sean McGinty, Sean McKee, Roger M Wadsworth, and Christopher McCormick. Modeling arterial wall drug concentrations following the insertion of a drug-eluting stent. *SIAM Journal on Applied Mathematics*, 73:2004–2028, 2013.

[39] James E Moore and Joel L Berry. Fluid and solid mechanical implications of vascular stenting. *Annals of biomedical engineering*, 30:498–508, 2002.

[40] Stefano Morlacchi and Francesco Migliavacca. Modeling stented coronary arteries: where we are, where to go. *Annals of biomedical engineering*, 41:1428–1444, 2013.

[41] Lazaros Papamanolis, Hyun Jin Kim, Clara Jaquet, Matthew Sinclair, Michiel Schaap, Ibrahim Danad, Pepijn van Diemen, Paul Knaapen, Laurent Najman, Hugues Talbot, et al. Myocardial perfusion simulation for coronary artery disease: a coupled patient-specific multiscale model. *Annals of biomedical engineering*, 49:1432–1447, 2021.

[42] S. Perotto and A. Zilio. Space-time adaptive hierarchical model reduction for parabolic equations. *Advanced modeling and simulation in engineering sciences*, 2:25, 2015.

[43] Simona Perotto. A survey of Hierarchical Model (Hi-Mod) reduction methods for elliptic problems. In *Numerical Simulations of Coupled Problems in Engineering*, pages 217–241. Springer, 2014.

[44] Simona Perotto, Gloria Bellini, Francesco Ballarin, Karol Calò, Valentina Mazzi, and Umberto Morbiducci. Isogeometric hierarchical model reduction for advection-diffusion process simulation in microchannels. In *Reduced Order Models for the Biomechanics of Living Organs*, Biomechanics of Living Organs, pages 197–211. Academic Press, 2023.

[45] Simona Perotto, Alexandre Ern, and Alessandro Veneziani. Hierarchical local model reduction for elliptic problems: a domain decomposition approach. *Multiscale Modeling & Simulation*, 8:1102–1127, 2010.

[46] Simona Perotto and Alessandro Veneziani. Coupled model and grid adaptivity in hierarchical reduction of elliptic problems. *Journal of Scientific Computing*, 60:505–536, 2014.

[47] Giuseppe Pontrelli and Filippo de Monte. Mass diffusion through two-layer porous media: an application to the drug-eluting stent. *International Journal of Heat and Mass Transfer*, 50:3658–3669, 2007.

[48] Alfio Quarteroni, Andrea Manzoni, and Federico Negri. *Reduced basis methods for partial differential equations*, volume 92. Springer, 2016.

[49] A. Ranno, K. Manjunatha, A. Glitz, N. Schaaps, S. Reese, F. Vogt, and M. Behr. In-silico analysis of hemodynamic indicators in idealized stented coronary arteries for varying stent indentation. *Computer Methods in Biomechanics and Biomedical Engineering*, pages 1–22, 2024.

[50] Anna Ranno, Kiran Manjunatha, Thore Koritzius, Ivo Steinbrecher, Norbert Hosters, Maximilian Nachtsheim, Pakhwan Nilcham, Nicole Schaaps, Anne Turoni-Glitz, Janina Datz, et al. A computational model of coronary arteries with in-stent restenosis coupling hemodynamics and pharmacokinetics with growth mechanics. *Scientific Reports*, 15:39229, 2025.

[51] Francesco Regazzoni. An optimally convergent fictitious domain method for interface problems. *Computer Methods in Applied Mechanics and Engineering*, 431:117327, 2024.

[52] RM Romarowski, Elena Faggiano, M Conti, A Reali, S Morganti, and F Auricchio. A novel computational framework to predict patient-specific hemodynamics after tevar: integration of structural and fluid-dynamics analysis by image elaboration. *Computers & Fluids*, 179:806–819, 2019.

[53] Charles A Taylor, Kersten Petersen, Nan Xiao, Matthew Sinclair, Ying Bai, Sabrina R Lynch, Adam UpdePac, and Michiel Schaap. Patient-specific modeling of blood flow in the coronary arteries. *Computer Methods in Applied Mechanics and Engineering*, 417:116414, 2023.

[54] Paolo Zunino, Carlo D'Angelo, Lorenza Petrini, Christian Vergara, Claudio Capelli, and Francesco Migliavacca. Numerical simulation of drug eluting coronary stents: mechanics, fluid dynamics and drug release. *Computer Methods in Applied Mechanics and Engineering*, 198:3633–3644, 2009.

[55] Paolo Zunino, Josip Tambača, Elena Cutrì, Suncica Čanić, Luca Formaggia, and Francesco Migliavacca. Integrated stent models based on dimension reduction: review and future perspectives. *Annals of biomedical engineering*, 44:604–617, 2016.

MOX Technical Reports, last issues

Dipartimento di Matematica
Politecnico di Milano, Via Bonardi 9 - 20133 Milano (Italy)

04/2026 Ragni, A.; Cavinato, L.; Ieva, F.
Penalized Likelihood Optimization for Adaptive Neighborhood Clustering in Time-to-Event Data with Group-Level Heterogeneity

03/2026 Mapelli, A.; Carini, L.; Ieva, F.; Sommariva, S.
A neighbour selection approach for identifying differential networks in conditional functional graphical models

02/2026 Antonietti, P.F.; Beirao da Veiga, L.; Botti, M.; Harnist, A.; Vacca, G.; Verani, M.
Virtual Element methods for non-Newtonian shear-thickening fluid flow problems

01/2026 Iapaolo V.; Vergani, A.M.; Cavinato, L.; Ieva, F.
Multi-view learning and omics integration: a unified perspective with applications to healthcare

Iapaolo, V.; Vergani, A.; Cavinato, L.; Ieva, F.
Multi-view learning and omics integration: a unified perspective with applications to healthcare

82/2025 Varetti, E.; Torzoni, M.; Tezzele, M.; Manzoni, A.
Adaptive digital twins for predictive decision-making: Online Bayesian learning of transition dynamics

81/2025 Leimer Saglio, C. B.; Pagani, S.; Antonietti, P. F.
A massively parallel non-overlapping Schwarz preconditioner for PolyDG methods in brain electrophysiology

79/2025 Zacchei, F.; Conti, P.; Frangi, A.; Manzoni, A.
Multi-Fidelity Delayed Acceptance: hierarchical MCMC sampling for Bayesian inverse problems combining multiple solvers through deep neural networks

78/2025 Botti, M.; Mascotto, L.
Trace inequalities for piecewise W^1,p functions over general polytopic meshes

77/2025 Bonetti, S.; Botti, M.; Vega, P.
A robust fully-mixed finite element method with skew-symmetry penalization for low-frequency poroelasticity